Observation of the sub-100 fs population of a dark state in a thiobase mediating intersystem crossing

Rocío Borrego-Varillas[†,♯], Danielle C. Teles-Ferreira[‡,♯], Artur Nenov[§,♯], Irene Conti[§], Lucia Ganzer[†], Cristian Manzoni[†], Marco Garavelli[*,§], Ana Maria de Paula[*,‡] and Giulio Cerullo[*,†]

† IFN-CNR, Dipartimento di Fisica, Politecnico di Milano, Piazza Leonardo da Vinci 32, I-20133 Milano, Italy

‡ Departamento de Física, Universidade Federal de Minas Gerais, 31270-901 Belo Horizonte-MG, Brazil

§ Dipartimento di Chimica Industriale, Università degli Studi di Bologna, Viale del Risorgimento 4, I-40136 Bologna, Italy

Contents

1 Theoretical background and protocols for acquisition of simulation parameters

1.1 QM/MM calculations: geometry refinement and electronic structure computations

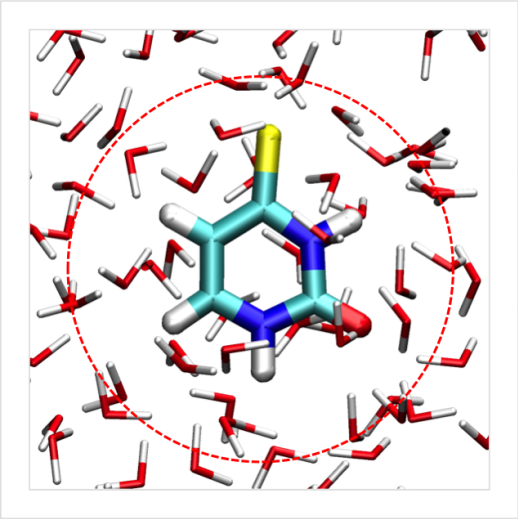

Figure S1: High/Medium/Low layer paritioning of 4-thiouracil in the QM/MM protocol. The High layer comprises the thiouracil, the Medium layer comprises all waters in 3 Å distance of the QM region (encircled with a dashed line). The rest of waters are included in the Low layer.

1.2 Non-adiabatic mixed quantum-classical dynamics simulations at the CASPT2 level

Gradients were computed numerically through a two-point finite differentiation formula using the COBRAMM's parallel environment. To speed up the numerical computations of the SS-RASPT2 gradients we made use of the fact that the perturbative correction is applied independently on each root. Thus, while at the reference point all states are corrected at SS-RASPT2 level, during the computation of the gradient only the state that drives the nuclear dynamics (i.e. the photoactive state) was taken into account. Care was taken for possible state swapping at each displaced geometry in case of near-degeneracy at the RASSCF level by following the nature of the wave function. The stability of the simulations was monitored through COBRAMM routines. If

a) an element the numerical gradient exceed a threshold (default 0.5)

b) the ratio of the lengths of the gradient vectors at two consecutive steps (i.e. $||g(t)||/||g(t-dt)||$) and, at the same time, the deviation of the total energy from its value at the previous step (i.e. $E_{tot}(t)-E_{tot}(t-dt)$) exceed certain thresholds (defaults 1.3 and 0.5 kcal/mol, respectively)

c) a single point computation fails to converge

the gradient is discarded and the Velocity Verlet step is repeated at the last stable geometry, first with a half step (in this case 0.5 fs) and, if the thresholds are exceeded again, with a double step (in this case 2.0 fs). Following the THS scheme the expression for the time-derivative coupling (TDC)

$$\sigma_{ij} = \frac{dR}{dt} d_{ij} = \frac{dR}{dt} \underbrace{\left\langle \Psi_i(r,t) \middle| \frac{d}{dR} \Psi_j(r,t) \right\rangle}_{NAC} = \underbrace{\left\langle \Psi_i(r,t) \middle| \frac{d}{dt} \Psi_j(r,t) \right\rangle}_{TDNAC} \tag{1}$$

is approximated to finite differences and the change in the electronic wave functions is resolved by computing overlap integrals between the adiabatic wave functions at different time steps. COBRAMM generalizes the TDC formulation of Barbatti (eq. 9 in ref. [Pit09]) to arbitrary time steps Δt:

$$\begin{aligned} \sigma_{ij} = \frac{1}{2\Delta t_{old}} \left(1 - \frac{0.5\Delta t_{old} + \Delta t}{0.5\Delta t_{old} + 0.5\Delta t} \right) & (\left\langle \Psi_i(t-\Delta t) \middle| \Psi_j(t-\Delta t-\Delta t_{old}) \right\rangle - \\ & \left\langle \Psi_j(t-\Delta t) \middle| \Psi_i(t-\Delta t-\Delta t_{old}) \right\rangle) + \\ \frac{1}{2\Delta t} \left(\frac{0.5\Delta t_{old} + \Delta t}{0.5\Delta t_{old} + 0.5\Delta t} \right) & (\left\langle \Psi_i(t) \middle| \Psi_j(t-\Delta t) \right\rangle - \\ & \left\langle \Psi_j(t) \middle| \Psi_i(t-\Delta t) \right\rangle) \end{aligned} \tag{2}$$

where Δt and Δt old are the time steps used to propagate the TDSE between step $i-1$ and i, as well as between step $i-2$ and $i-1$. Note that eq. 2 simplifies to eq. 9 in ref. [Pit09] when $\Delta t_{old} = \Delta t$. The individual terms are obtained from wave function overlaps, which at present are computed at the RASSCF level (i.e. using the RASSCF wavefunctions) through the RASSI utility [Mal86] of Molcas and further scaled by the ratio of the SS-RASPT2 and RASSCF energy gaps $(E_j^{CASSCF} - E_i^{CASSCF})/(E_j^{SSPT2} - E_i^{SSPT2}))$, which

follows from the relation:

$$\begin{aligned}\sigma_{ij} =& \big\langle \Psi_i(t)^{SSPT2} \big| \frac{d}{dt} \Psi_j(t)^{SSPT2} \big\rangle = \frac{dR}{dt} \big\langle \Psi_i(t)^{SSPT2} \big| \frac{d}{dR} \Psi_j(t)^{SSPT2} \big\rangle = \\ & v \cdot d_{ij}^{SSPT2} = v \cdot \frac{\big\langle \Psi_i(t)^{SSPT2} \big| \nabla_R \hat{H} \big| \Psi_j(t)^{SSPT2} \big\rangle}{E_j^{SSPT2} - E_i^{SSPT2}} \approx \\ & v \cdot \frac{\big\langle \Psi_i(t)^{CASSCF} \big| \nabla_R \hat{H} \big| \Psi_j(t)^{CASSCF} \big\rangle}{E_j^{CASSCF} - E_i^{CASSCF}} \cdot \frac{E_j^{CASSCF} - E_i^{CASSCF}}{E_j^{SSPT2} - E_i^{SSPT2}} = \\ & v \cdot d_{ij}^{CASSCF} \cdot \frac{E_j^{CASSCF} - E_i^{CASSCF}}{E_j^{SSPT2} - E_i^{SSPT2}}\end{aligned} \tag{3}$$

In the chain following equality is assumed:

$$\big\langle \Psi_i(t)^{SSPT2} \big| \nabla_R \hat{H} \big| \Psi_j(t)^{SSPT2} \big\rangle \approx \big\langle \Psi_i(t)^{CASSCF} \big| \nabla_R \hat{H} \big| \Psi_j(t)^{CASSCF} \big\rangle \tag{4}$$

Effectively, when the SS-RASPT2 correction to the SA-CASSCF energies decreases the energy gap between a pair of states the value of the time-derivative coupling is increased uniformly. In the particular application, the bright $\pi\pi^*$ and dark $n\pi^*$ states are always well separated at the RASSCF level due to the difficulty of the RASSCF method to describe at the same footing both states, with the $n\pi^*$ state being lower in energy. Correspondingly, the non-adiabatic coupling which controls the $\pi\pi^* \rightarrow n\pi^*$ decay is comparably small. SS-RASPT2 lowers the energy of $\pi\pi^*$ state so that it approaches the $n\pi^*$ state. The scaling factor introduced above assures that in such cases the non-adiabatic coupling of the two states increases (linearly with the decreasing energy gap) as the states are expected to mix when they become near-degenerate. In addition, a wave function following algorithm allows to identify state swapping (such as at crossings) at the SS-CASPT2 level. The THS scheme allows to work with relatively large time steps (such as 1.0 fs) even in the region of $\pi\pi^*/n\pi^*$ near-degeneracy and state swapping. Tully's fewest switches surface hopping algorithm is know to suffer from artificial coherence effects. A decoherence correction, originally proposed by Truhlar and co-workers [Zhu05] and realized by Persico et al. [Gra07] is used in the present case as a countermeasure. Kinetic energy scaling (for total energy conservation) after a hopping event is performed along the velocity vector. The generally contracted basis set ANO-L adopting contractions 4s3p2d1f on sulfur, 3s2p1d on carbon, oxygen and nitrogen and 2s1p on hydrogen was utilized.

1.3 Simulation protocol for non-linear spectroscopy

The pump probe (PP) signal $W^{(3)}(t_2, \Omega_3)$ can be seen formally as the marginal of the Fourier transform of the third-order signal $S^{(3)}(t_1, t_2, t_3)$ [Muk95, Muk04, Abr09, Ham11, Abr07].

$$W^{(3)}(t_2, \Omega_3) = \int_{-\infty}^{\infty} dt_1 \int_{0}^{\infty} dt_3 \; S^{(3)}(t_1, t_2, t_3) \; e^{i\Omega_3 t_3} \delta(t_1). \tag{5}$$

In the following we will elaborate on the simulation protocol for $S^{(3)}(t_1, t_2, t_3)$, thus covering PP and two-dimensional (2D) nonlinear experiments. $S^{(3)}(t_1, t_2, t_3)$ is the convolution of the third order nonlinear response of the system $R^{(3)}(t_1, t_2, t_3)$ due to the interaction with three incident laser pulses with wave vectors k_1, k_2 and k_3

$$\begin{aligned} S^{(3)}(t_1, t_2, t_3) = \int_{-\infty}^{\infty} dt \int_{0}^{\infty} dt_1 \int_{0}^{\infty} dt_2 \int_{0}^{\infty} dt_3 \; R^{(3)}(t_1, t_2, t_3) \times \\ \mathbf{E}(r,t)\mathbf{E}(r,t-t_1)\mathbf{E}(r,t-t_1-t_2)\mathbf{E}(r,t-t_1-t_2-t_3) \end{aligned} \tag{6}$$

with pulses $\mathbf{E}(r,t) = E(t)e^{ikr-i\omega t}$ with central frequency ω and complex envelope $E(t)$. Assuming temporally well separated ultrashort laser pulses (impulsive limit, i.e. the limit in which the pulse duration is less than a single vibrational oscillation period) the nonlinear response of the system $R^{(3)}(t_1, t_2, t_3)$ becomes equivalent to the third-order signal $S^{(3)}(t_1, t_2, t_3)$. In section 1.3.7 the influence of the pulse duration on the spectra is demonstrated.

$R^{(3)}(t_1, t_2, t_3)$ can be written in terms of the perturbation of the system's density matrix by three external optical electric fields (the interaction with the optical filed being described in the impulsive limit through the coordinate dependent transition dipole moment operator $\hat{\boldsymbol{\mu}} = \sum_{ij} \mu_{ij} |i\rangle\langle j|$) and the field-free evolution of the density matrix during the intervals t_1, t_2 and t_3 between the pulses:

$$R^{(3)}(t_1, t_2, t_3) = (i)^3 Tr \left[\hat{\boldsymbol{\mu}} \mathbb{G}(t_3) \left[\hat{\boldsymbol{\mu}}, \mathbb{G}(t_2) \left[\hat{\boldsymbol{\mu}}, \mathbb{G}(t_1) \left[\hat{\boldsymbol{\mu}}, \rho(0)\right]\right]\right]\right] \tag{7}$$

giving rise to eight independent contributions (Liouville pathways). $\rho(t)$ is the time-dependent density matrix of the system, being in the ground state (GS) at equilibrium before the interaction with the first pulse (i.e. $\rho(0) = |g\rangle\langle g|$). For the electronic states i we consider the GS g, the manifold of singly excited states (ESs) e, e', accessible with the pump pulse (pair) and the manifold of higher lying states f, accessible through the probe pulse. $\mathbb{G}(t)\rho(t) = e^{-i\hat{H}t}\rho(0)e^{i\hat{H}t}$ the retarded Green's function, describes the field-free system propagation governed by the vibronic Hamiltonian $\hat{H}$. The nonlinear response $R^{(3)}(t_1, t_2, t_3)$ depends on the spatial orientation of the wave

vectors of the incident pulses, i.e. is emitted in a given phase-matched direction. By adjusting the experimental set up (boxcar arrangement, collinear pump pulse arrangement) one can selectively detect sub-groups of Liouville pathways. For example, the rephasing nonlinear response $R^{(3)}_{\mathbf{k_I}}(t_1, t_2, t_3)$

$$R^{(3)}_{\mathbf{k_I}}(t_1, t_2, t_3) = \sum_{i=GSB,SE,ESA} R^{(3)}_{\mathbf{k_I},i}(t_1, t_2, t_3) \tag{8}$$

is emitted in the so called rephasing phase-matching direction ($\boldsymbol{k_I} = -k_1 + k_2 + k_3$) and includes three possible interaction sequences of the incident electric fields with the system denoted as ground state bleach (GSB), excited state absorption (ESA) and stimulated emission (SE). Similarly, the nonrephasing nonlinear response can be obtained in the phase-matching direction $\boldsymbol{k_{II}} = +k_1 - k_2 + k_3$. The pump-probe response can be obtained either in the rephasing or in the nonrephasing directions which become identical when $t_1 = 0$.

1.3.1 Cumulant expansion of Gaussian fluctuations and line shape functions

Eq. 7 can be solved using second-order cumulant expansion within the framework of linear coupling of the system's energies to a Gaussian bath. This is known as the cumulant expansion of Gaussian fluctuations (CGF). It allows to calculate the shapes of electronic transition bands coupled to a bath for fluctuations with arbitrary time scales by using the formalism of line shape functions [Muk04, Abr07]. In the following we describe a bath with both fast and slow modes, i.e. modes that adjust themselves quickly and such that cause long-range memory effects. The Markovian approximation (memorylessness) is applied to the fast modes. During t_1 and t_3, these cause homogeneous line broadening, while during t_2 they induce population relaxation. In the limit of decoupled populations and coherences (secular approximation of the Green's function) the population relaxation is described by the Pauli master equation:

$$\dot{\rho_{ee}}(t) = -\sum_{e'} K_{e'e',ee}\rho_{e'e'}(t) \tag{9}$$

with $\boldsymbol{K}$ the rate matrix with elements $K_{e'e',ee}$ depicting the population transfer rate from state e into state e' which is taken to be independent of the fluctuations of the slow modes. The solution of the differential equation is formally given by the population Green's function $\rho_{e'e'}(t) = \sum_e \boldsymbol{G}_{e'e',ee}(t)\rho_{ee}(0)$ and the elements of the matrix $\boldsymbol{G}$ act as time-dependent weighting factors

in the population pathways describing ESA and SE (see eq. 10). The slow bath modes are responsible for spectral diffusion during all three intervals t_1, t_2, and t_3, causing correlations during the three intervals. The secular approximation allows to further partition the nonlinear response (eq. 8) into population ($e' = e$ during delay time t_2) and coherence contributions ($e' \neq e$ during delay time t_2). The population contributions then read:

$$\begin{aligned}
R^{(3)}_{\mathbf{k_I},\mathrm{ESA,i}} =& + i \sum_{e',e,f} \mu^2_{fe'}\mu^2_{ge}\ \boldsymbol{G}_{e'e',ee}(t_2)\times \\
& e^{-i(\varepsilon_f - \varepsilon_{e'})t_3 + i(\varepsilon_e - \varepsilon_g)t_1 + \varphi^{ESA,i}_{fe'e}(t_1, t_1{+}t_2, t_1{+}t_2{+}t_3, 0)} \\
R^{(3)}_{\mathbf{k_I},\mathrm{SE,i}} =& - i \sum_{e',e} \mu^2_{ge'}\mu^2_{ge}\ \boldsymbol{G}_{e'e',ee}(t_2)\times \\
& e^{-i(\varepsilon_{e'} - \varepsilon_g)t_3 + i(\varepsilon_e - \varepsilon_g)t_1 + \varphi^{SE,i}_{ege'}(0, t_1{+}t_2, t_1{+}t_2{+}t_3, t_1)} \\
R^{(3)}_{\mathbf{k_I},\mathrm{GSB}} =& - i \sum_{e',e} \mu^2_{ge'}\mu^2_{ge}\times \\
& e^{-i(\epsilon_{e'} - \varepsilon_g)t_3 + i(\epsilon_e - \varepsilon_g)t_1 + \varphi^{GSB}_{ege'}(0, t_1, t_1{+}t_2{+}t_3, t_1{+}t_2)}.
\end{aligned} \tag{10}$$

The coherence contributions read:

$$\begin{aligned}
R^{(3)}_{\mathbf{k_I},\mathrm{ESA,ii}} =& + i \sum_{e',e}^{e'\neq e} \sum_{f} \mu_{fe'}\mu_{fe}\mu_{ge'}\mu_{ge}\ e^{-i(\varepsilon_f - \varepsilon_e)t_3}\times \\
& e^{-i(\varepsilon_{e'} - \varepsilon_e)t_2 + i(\varepsilon_e - \varepsilon_g)t_1 + \varphi^{ESA,ii}_{fe'e}(t_1, t_1{+}t_2, t_1{+}t_2{+}t_3, 0)} \\
R^{(3)}_{\mathbf{k_I},\mathrm{SE,ii}} =& - i \sum_{e',e}^{e'\neq e} \mu^2_{ge'}\mu^2_{ge}\ e^{-i(\varepsilon'_e - \varepsilon_g)t_3}\times \\
& e^{-i(\varepsilon_{e'} - \varepsilon_e)t_2 + i(\varepsilon_e - \varepsilon_g)t_1 + \varphi^{SE,ii}_{e'ge}(0, t_1{+}t_2, t_1{+}t_2{+}t_3, t_1)}.
\end{aligned} \tag{11}$$

As there is only a single GS, no coherence contribution is observed for the GSB. In eqs. 10-11 ε_i ($i \in \{g, e, f\}$) is the electronic contribution to the energy of the i-th ES (the energy of the GS $\varepsilon_g = 0$ is used as a reference). $\varphi(t_4, t_3, t_2, t_1)$ are phase functions that describe the coupling to the bath and,

hence, give rise to the time-dependent spectral line shapes [Abr07, Abr09].

$$\begin{aligned}
\varphi^{ESA,i}_{fe'e}(t_1, t_1{+}t_2, t_1{+}t_2{+}t_3, 0) &= \delta_{e'e} f^{(C),*}_{efe}(t_1, t_1{+}t_2, t_1{+}t_2{+}t_3, 0) \\
&\quad + \xi_{e'e} f^{(I),*}_{fe'e'e}(t_3, t_2, t_1) \\
\varphi^{SE,i}_{ege'}(0, t_1{+}t_2, t_1{+}t_2{+}t_3, t_1) &= \delta_{e'e} f^{(C)}_{ege}(0, t_1{+}t_2, t_1{+}t_2{+}t_3, t_1) \\
&\quad + \xi_{e'e} f^{(I),*}_{e'ge'e}(t_3, t_2, t_1) \\
\varphi^{GSB}_{ege'}(0, t_1, t_1{+}t_2{+}t_3, t_1{+}t_2) &= \delta_{e'e} f^{(C)}_{ege'}(0, t_1, t_1{+}t_2{+}t_3, t_1{+}t_2)
\end{aligned} \tag{12}$$

$$\begin{aligned}
\varphi^{ESA,ii}_{fe'e}(t_1, t_1{+}t_2, t_1{+}t_2{+}t_3, 0) &= f^{(C),*}_{e'fe}(t_1, t_1{+}t_2, t_1{+}t_2{+}t_3, 0) \\
\varphi^{SE,ii}_{ege'}(0, t_1{+}t_2, t_1{+}t_2{+}t_3, t_1) &= f^{(C)}_{e'ge}(0, t_1{+}t_2, t_1{+}t_2{+}t_3, t_1)
\end{aligned}$$

where $\xi_{e'e} = 1 - \delta_{e'e}$. The phase functions of the population contributions to the ESA and SE signals ($\varphi^{ESA,i}$ and $\varphi^{SE,i}$) have both a coherent ($f^{(C)}_{cba}$) and incoherent ($f^{(I)}_{cbe'e}$) part, the former comprising population-conserving Liouville pathways, the latter population-transfer pathways with the Markovian approximation for the fast modes. Both functions include correlations between t_1, t_2 and t_3. The coherent function $f^{(C)}_{cba}$ reads:

$$\begin{aligned}
f^{(C)}_{cba}(\tau_4, \tau_3, \tau_2, \tau_1) = &- g_{cc}(\tau_{43}) - g_{bb}(\tau_{32}) - g_{aa}(\tau_{21}) \\
&- g_{cb}(\tau_{42}) + g_{cb}(\tau_{43}) + g_{cb}(\tau_{32}) \\
&- g_{ca}(\tau_{41}) + g_{ca}(\tau_{42}) + g_{ca}(\tau_{31}) - g_{ca}(\tau_{32}) \\
&- g_{ba}(\tau_{31}) + g_{ba}(\tau_{32}) + g_{ba}(\tau_{21})
\end{aligned} \tag{13}$$

with $\tau_{ij} = \tau_i - \tau_j$. The incoherent function $f^{(I)}_{cbe'e}$ reads:

$$\begin{aligned}
f^{(I)}_{cbe'e}(t_3, t_2, t_1) = &- g_{ee}(t_1) - g_{bb}(t_3) - g^*_{cc}(t_3) \\
&- g_{be}(t_1 + t_2 + t_3) + g_{be}(t_1 + t_2) + g_{be}(t_2 + t_3) - g_{be}(t_2) \\
&+ g_{ce}(t_1 + t_2 + t_3) - g_{ce}(t_1 + t_2) - g_{ce}(t_2 + t_3) + g_{ce}(t_2) \\
&+ g_{cb}(t_3) + g^*_{bc}(t_3) \\
&+ 2i\mathrm{Im}[+g_{ce'}(t_2 + t_3) - g_{ce'}(t_2) - g_{ce'}(t_3) \\
&\qquad - g_{be'}(t_2 + t_3) + g_{be'}(t_2) + g_{be'}(t_3)].
\end{aligned} \tag{14}$$

We note that the line shape functions $g_{be}(t)$ and $g_{ce}(t)$ vanish by construction in the case of pump probe spectroscopy simulations in which the first two light-matter interactions occur simultaneously (i.e. $t_1 = 0$). In the following

we use a simplified version of the incoherent function (eq. 14) which omits most of the terms to give:

$$f_{fe}^{(I)}(t_3, t_1) = -g_{ee}(t_1) - g_{ff}^{*}(t_3) \tag{15}$$

which depends only on the line shape function $g_{ee}(t_1)$ of the initial state and on the line shape functions $g_{ff}^{*}(t3)$ of the states coupled to the probe pulse. Physically, the above expression describes signals associated with the trapping of population in an excited state (i.e. e', the triplet manifold in this case) during the decay process on a time scale facilitating the dissipation of excess vibrational energy in the environment (so called vibrational cooling). In such case, the spectrum is dominated by the electronic structure of the equilibrium geometry of the trapping state. Within this framework the dynamics during t_3 can be calculated with the e' Hamiltonian as reference, thus effectively eliminating all terms depending on e'. Effectively, eq. 15 decouples the vibrational dynamics in the triplet states from that in the afore populated $n\pi^*$ state. This is clearly an approximation to the actual dynamics in the sub-ps regime, as energy dissipation has not occurred yet and the ESA line shape potentially depends on dynamics in the triplet manifold. However, we note that the line shape of the experimentally recorded ESA signal does not show any intensity beat pattern, thus suggesting an incoherent inter-system crossing mechanism and supporting work in the Markovian limit. The incoherent dynamics in the triplet manifold would lead to a signal broadening which can be taken into consideration in a phenomenological fashion.

In the particular application to 4-thiouracil we simulate only the contribution of the SE from the $\pi\pi^*$ state to the overall signal at early times as ground state bleach falls outside of the spectral window and ESA features of the $\pi\pi^*$ state are not considered at this point. The $n\pi^*$ state shows neither SE, not ESA features. At later times the only spectral contribution arises through ESA from the triplet manifold represented by the $^3\pi\pi^*$ and $^3n\pi^*$ states. Thus, the overall signal consists of the coherent function of eq. 12,SE,i and the (simplified) incoherent function of eq. 12,ESA,i.
$g_{ij}(t)$ in eqs. 13-14 is the line shape function, which is an integral transformation of the autocorrelation function of bath fluctuations $C_{ij}(t)$ [Muk95, Muk09]:

$$g_{ij}(t) = \frac{1}{2\pi} \int \frac{C_{ij}(\omega)}{\omega^2} [\coth\left(\frac{\hbar\omega}{2k_BT}\right)(1 - \cos\omega t) + i\sin\omega t - i\omega t]\, d\omega. \tag{16}$$

In the case when the system is coupled to a set of high-frequency (intramolecular) modes and a continuum of low-frequency (intra- and intermolecular) modes the spectral density can be partitioned into: a) a weakly undamped

or underdamped contribution due to the slowly decaying correlation function due to high-frequency modes, responsible for vibrational progressions in the spectra; b) an overdamped contribution due to the fast-decaying correlation function associated with the low-frequency modes responsible for the homogeneous broadening of the signals. The total line shape function then contains two parts as well [Val16]. The semi-classical overdamped regime is usually represented by the line shape function of the semi-classical Brownian oscillator (OBO) in the high-temperature limit [Muk95, Li94, But12]:

$$g_{ij}^{\mathrm{OBO}}(t) = \frac{\lambda_{ij}}{\Lambda}\left(\frac{2k_BT}{\hbar\Lambda} - i\right)(e^{-\Lambda t} + \Lambda t - 1). \tag{17}$$

In eq. 17 λ_{ij} and Λ^{-1} are the system-bath coupling strength and the fluctuation time scale, respectively.

Undamped vibrations are described through the line shape function of the multidimensional uncoupled displaced harmonic oscillator (DHO)[Muk95]:

$$g_{ij}^{\mathrm{DHO}}(t) = \sum_k \frac{\omega_k \tilde{d}_{ik}\tilde{d}_{jk}}{2}\left[\coth\left(\frac{\omega_k}{2k_BT}\right)(1-\cos(\omega_k t)) + i\sin(\omega_k t)\right] \tag{18}$$

with ω_k the frequency and $\tilde{d}_{ik}$ the displacement of the i-th electronic potential along the k-th mass-weighted normal mode (Figure S2). The state-specific displacements $\tilde{d}_{ik}$ determine the magnitude of diagonal correlation functions $C_{ii}(t)$ and are related to spectroscopic parameters like the Huang-Rhys factors S_{ik} or the reorganization energy λ_{ik} through the following relations:

$$S_{ik} = \frac{\tilde{d}_{ik}^2\omega_k}{2\hbar} \qquad \text{and} \qquad \lambda_{ik} = \frac{\tilde{d}_{ik}^2\omega_k^2}{2\hbar}. \tag{19}$$

and can be used to compute the spectral densities either in the undamped ($C^{(u)}$ or damped $C^{(d)}$ regimes [But12]:

$$C^{\mathrm{u}}(w) = \sum_i \pi\ S_{ik}\ \omega_k^2\left[\delta(\omega-\omega_k)\right] \quad \text{and} \quad C^{\mathrm{d}}(w) = \sum_i \frac{2\sqrt{2}\ S_{ik}\ \omega_k^3\ \omega\ \gamma}{(\omega^2-\omega_k^2)^2 + 2\gamma^2\omega^2)} \tag{20}$$

where γ is a damping factor. Cross-correlation functions $C_{ij}(t)$ depend on the displacements $\tilde{d}_{ik}$ and $\tilde{d}_{jk}$ associated with two transitions. Because negative displacements (with respect to the GS, Figure S2) are allowed, the corresponding spectral densities $C_{ij}(w)$ that can be formulated following eqs. 19 and 20 can have negative contributions[Nem10] (see next section).

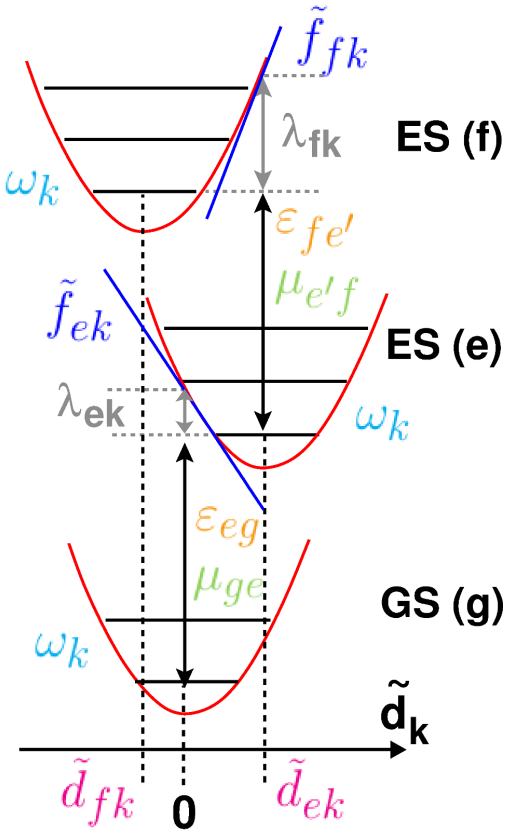

Figure S2: Displaced harmonic oscillator model for a three level system.

1.3.2 Solving the Pauli master equation: population dynamics

The system under study presents only one state under the envelope of the pump pulse ($\sim 325 - 345$ nm). This is the first bright singlet $\pi\pi^*$ state of 4-thiouracil and the second excited state in the FC region. Utilizing the outcome of the analysis of the potential energy surfaces and molecular dynamics simulations we elaborated a sequential model that describes the population decay following excitation of the $\pi\pi^*$ state. Based on non-adiabatic mixed quantum-classical molecular dynamics simulations at the SS-RASPT2/SA-3-RASSCF$(12, 9|2, 4)$ level we obtain a lifetime of the $^1\pi\pi^*$ state of 67.5 fs (see sec. 2.4) which is within the error range of the experimental lifetime of 76 ± 16 fs. Global analysis of the experimental data gives a 225 ± 30 fs time constant for the build up of the fingerprint ESA signal of the triplet state, which is thus assigned to the lifetime of the intermediate dark $^1n\pi^*$ state. The sequential model describing the dynamics in near-UV excited

4-thiouracil is:

$$^1\pi\pi^* \xrightarrow{k_{^1\pi\pi^*}} {}^1n\pi^* \xrightarrow{k_{^1n\pi^*}} {}^3\pi\pi^*$$

Equation 21 shows the rate matrix corresponding to this model

$$\mathbf{K} = \begin{array}{c} \\ \rho_{^3(\pi|n)\pi^*} \\ \rho_{^1n\pi^*} \\ \rho_{^1\pi\pi^*} \end{array} \begin{array}{c} \begin{array}{ccc} \rho_{^3(\pi|n)\pi^*} & \rho_{^1n\pi^*} & \rho_{^1\pi\pi^*} \end{array} \\ \begin{bmatrix} +k_{^3(\pi|n)\pi^*} & -k_{^1n\pi^*} & 0 \\ 0 & +k_{^1n\pi^*} & -k_{^1\pi\pi^*} \\ 0 & 0 & +k_{^1\pi\pi^*} \end{bmatrix} \end{array} \tag{21}$$

where the rates $k_{^1\pi\pi^*} = 1/76$ fs^{-1}, $k_{^1n\pi^*} = 1/225$ fs^{-1} were taken as the reciprocal lifetimes. The rate of the depopulation of the triplet manifold $k_{^3(\pi|n)\pi^*}$ is set to $k_{^3(\pi|n)\pi^*} = 1/\infty$ fs^{-1}. Solving the Pauli master equation (eq. 9) we obtain following expressions for the population dynamics:

$$\begin{aligned} \rho_{^1\pi\pi^*}(t) =& e^{-k_{^1\pi\pi^*}t} \\ \rho_{^1n\pi^*}(t) =& \frac{k_{^1\pi\pi^*}}{-k_{^1\pi\pi^*} + k_{^1n\pi^*}}(e^{-k_{^1\pi\pi^*}t} - e^{-k_{^1n\pi^*}t}) \\ \rho_{^3(\pi|n)\pi^*}(t) =& \frac{-k_{^1n\pi^*}}{-k_{^1\pi\pi^*} + k_{^1n\pi^*}}(e^{-k_{^1\pi\pi^*}t} - 1) + \frac{k_{^1\pi\pi^*}}{-k_{^1\pi\pi^*} + k_{^1n\pi^*}}(e^{-k_{^1n\pi^*}t} - 1) \end{aligned} \tag{22}$$

The sequential model described above, shows the evolution of the population between 0 and 600 fs delay time starting in the $\pi\pi^*$ state ($\rho_{\pi\pi^*} = 1$). The population of the dark intermediate $n\pi^*$ state $\rho_{n\pi^*}$ shows a peak around 100 fs. After 600 fs ca. 90% of the population is the triplet manifold The density-matrix element $\rho_{^1\pi\pi^*}(t)$ appears as time-dependent weighting factor in front of the coherent part $f^{(C)}_{cba}$ of the population contribution $R^{(3)}_{\mathbf{k_I},\mathrm{SE,i}}$ (eq. 10) and causes the exponential decay of the signals associated with the $\pi\pi^*$ state. Due to the vanishing transition dipole moment of the GS$\leftarrow n\pi^*$ transition and the lack of intense ESA signals in the probed spectral window the $^1n\pi^*$ state can be seen as a "phantom" state which does not show in the spectra. The density-matrix element $\rho_{^3(\pi|n)\pi^*}(t)$ multiply the incoherent part $f^{(I)}_{cbe'e}$ of the population contributions and lead to the build-up of the triplet associated signals at times close to 200 fs. We remind that there is no incoherent contribution to the SE from the triplet manifold.
The $S_2(1\pi\pi^*) \rightarrow T_2(3n\pi^*) \rightarrow T_1(3\pi\pi^*)$ channel, which accounts for up to 25% of the population, has been neglected in this simulation. This has no effect on the spectral dynamics of the SE, which decays with the effective time constant of 78 fs describing the population splitting in $1n\pi^*$ and $3n\pi^*$, but it would affect slightly the dynamics of the triplet ESA as it would introduce at early times (sub-100 fs) a weak ESA signal in the red around 625 nm coming from the ultrafast population of the $3n\pi^*$ state from the $1\pi\pi^*$ state which

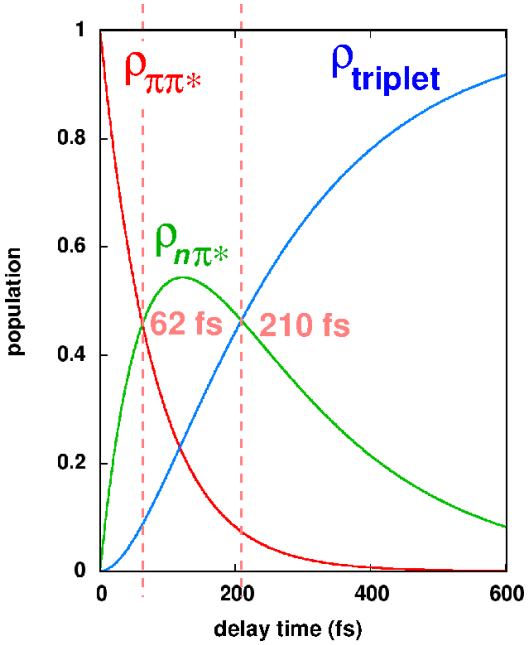

Figure S3: Population dynamics in near-UV excited 4-thiouracil.

would then blue-shift in the 550 nm due to the decay of the $3n\pi*$ state to the energetically lower lying $3\pi\pi^*$ state.

1.3.3 Spectral densities through gradient projection and normal mode analysis.

An expression for the displacements $\tilde{d}_{ik}$ can be obtained from the expression for the energy gap $\Delta E_{ij}(\tilde{q}_k)$ between states i and j in the displaced Harmonic oscillator model.

$$\Delta E_{ij}(\tilde{\boldsymbol{q}}) = \varepsilon_i - \varepsilon_j + \sum_k \left(\frac{1}{2}\omega_k^2(\tilde{d}_{ik}^2 - \tilde{d}_{jk}^2) - \omega_k^2(\tilde{d}_{ik} - \tilde{d}_{jk})\tilde{q}_k \right) \tag{23}$$

expressed in mass-weighted normal mode coordinates $\tilde{\boldsymbol{q}}$. $\varepsilon_i - \varepsilon_j$ is the adiabatic excitation energy between states i and j. When computed at the equilibrium of state j the gradient of the energy of state i equates the gradient of the energy gap

$$\nabla_{\tilde{\boldsymbol{q}}} \Delta E_{ij}(\tilde{\boldsymbol{q}}) = \nabla_{\tilde{\boldsymbol{q}}} E_i(\tilde{\boldsymbol{q}}) = \nabla_{\boldsymbol{Q}} E_i(\boldsymbol{Q})\ \nabla_{\tilde{\boldsymbol{q}}} \boldsymbol{Q} = \mathbb{P}^\dagger \mathbb{M}^{-\frac{1}{2}} \boldsymbol{f}_i \tag{24}$$

where $\mathbb{P}$ is a matrix whose columns are the normal modes of the system $\boldsymbol{\xi}_k$ expressed in normalized mass-weighted Cartesian coordinates $\boldsymbol{Q}$, $\mathbb{M}$ is

a diagonal matrix with the nuclear masses and $\boldsymbol{f}_i$ is the Cartesian energy gradient. Taking the derivative with respect to $\tilde{\boldsymbol{q}}$ in eq. 23 and inserting the expression derived in eq. 24 gives [Lee16, Fer12]

$$\tilde{\boldsymbol{d}}_{\boldsymbol{i}} = -\mathbb{W}^{-2}\mathbb{P}^{\dagger}\mathbb{M}^{-\frac{1}{2}}\boldsymbol{f}_i + \tilde{\boldsymbol{d}}_j \tag{25}$$

where $\tilde{\boldsymbol{d}}_i$ and $\tilde{\boldsymbol{d}}_j$ are k-dimensional arrays of the displacements along all modes on states i and j.

An alternative to the gradient projection technique is the normal mode analysis [Kur01]. Starting with the definition of the normal mode matrix (eq. 24)

$$\mathbb{P}^{\dagger} = \mathbb{M}^{\frac{1}{2}}\nabla_{\tilde{\boldsymbol{q}}}\boldsymbol{Q} \tag{26}$$

one can express it in terms of finite differences as

$$\mathbb{P}^{\dagger}\Delta\tilde{\boldsymbol{q}} = \mathbb{M}^{\frac{1}{2}}\Delta\boldsymbol{Q} \tag{27}$$

Thereby, $\Delta\tilde{\boldsymbol{q}}$ becomes the array of displacements $\tilde{\boldsymbol{d}}_{\boldsymbol{i}}$ along the normal modes of the system when the difference is taken with respect to the reference point on state i. Rearranging gives the final working equation

$$\tilde{\boldsymbol{d}}_i = \mathbb{P}^{-1}\mathbb{M}^{\frac{1}{2}}\Delta\boldsymbol{Q} \tag{28}$$

which allows to estimate how much every normal mode $\boldsymbol{\xi}_k$ has to be displaced to connect two points in Cartesian coordinate space. In eq. 28 $\Delta\boldsymbol{Q}$ is the difference in Cartesian coordinates between two geometries. With the normal mode analysis attention should be paid to global translational and rotational degrees of freedom which have to be removed prior to computing the difference in Cartesian coordinates. To this end we followed an iterative procedure relying on the vectors of inertia in order to minimize the distance in space between two geometries as outlined in ref. [Kur01b]. Furthermore, it is paramount that both geometries used to compute $\Delta\boldsymbol{Q}$ have been optimized at the same level of theory in order to avoid spurious contributions to the spectral densities.

1.3.4 Spectral densities of the singlet states $^1\pi\pi^*$ and $^1n\pi^*$.

Figure S4 shows the spectral densities of the lowest singlet states of 4-thiouracil, the bright $^1\pi\pi^*$ state (S4a) and the dark $^1n\pi^*$ state (S4b) constructed following eq. 20 with a weak damping factor γ of 5 cm^{-1}. This spectral density of $^1\pi\pi^*$ is eventually used to simulate the linear absorption (ocher in Figure S7) and the temporal evolution of the stimulated

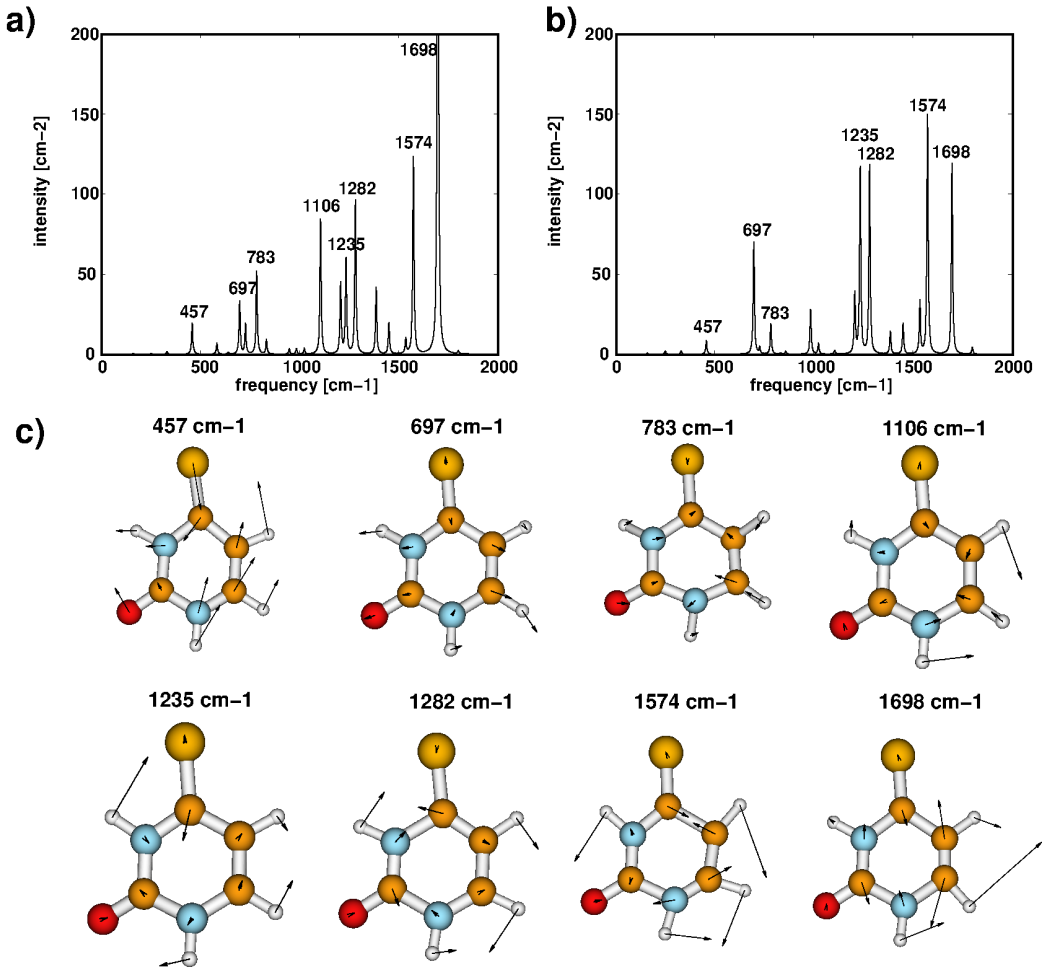

Figure S4: Spectral density of the lowest singlet states of 4-thiouracil. In (a) the bright $^1\pi\pi^*$ state, in (b) the dark $^1n\pi^*$ state. Most prominent normal modes are shown in (c). See also Table S1.

emission in Figures 1C and 1D of the main text. The Huang Rhys factors S_{ik} (subscript indicates the k-th normal mode of the i-th electronic state) that enter in the formula were obtained using displacements $\tilde{\boldsymbol{d}}_{ik}$ by means of the normal mode analysis outlined in sec. 1.3.3. Specifically, the difference in Cartesian coordinates between the ground state equilibrium geometry relaxed at the QM(MP2)/MM(AMBER) level and the relaxed geometry on each excited state (i.e. $\mathrm{Min}_{\pi\pi^*}$ or $\mathrm{Min}_{n\pi^*}$), optimized at the QM(MS-CASPT2/SA-3-CASSCF(12,9))/MM(AMBER) level of theory with an active space composed of all valence π-orbitals (Figure S6), was projected on the ground state normal modes of the system computed at the QM(MP2)/MM(AMBER) level. Thereby, Duschinsky rotations in the excited state were neglected. Coefficients are listed in Table S1. The spectral density of the $^1\pi\pi^*$ state is characterized three sets of normal modes. The low-frequency range (< 1000 cm^{-1}) exhibits three strong contributions, a ring breathing mode with a frequency of 457 cm^{-1} and two hydrogen-out-of-plane vibrations with frequencies 697 cm^{-1} and 783 cm^{-1}.

We note the nice agreement of the frequencies of the two most intense modes in with the 400 cm^{-1} and 680 cm^{-1} frequencies obtained after Fourier transforming the experimental pump probe signal (see Figure S23). The mid-frequency region ($1000 - 1300$ cm^{-1}) comprises hydrogen in-plane bending deformations with the 1106 cm^{-1}, 1235 cm^{-1} and 1282 cm^{-1} being the dominant modes. The 1282 cm^{-1} mode involves also a pronounced carbon-sulfur stretching. The high-frequency region (> 1300 cm^{-1}), on the other hand, is dominated by two carbon-carbon and carbon-nitrogen stretching modes with frequencies 1574 cm^{-1} and 1698 cm^{-1}. The mid- and high-frequencies remain unresolved experimentally as they fall outside of the resolution limit of the utilized 16 fs long pulses. The spectral density of the $^1n\pi*$ state is dominated by the same set of modes, with the 697 cm^{-1} and 1235 cm^{-1} modes gaining in magnitude, while the 783 cm^{-1}, 1106 cm^{-1} and 1698 cm^{-1} modes decrease in magnitude.

1.3.5 Spectral densities of the bright excited states accessible from the triplet states $^3\pi\pi^*$ and $^3\pi\pi^*$.

Figure S5 shows the spectral density of the higher lying bright triplet state accessible (i.e. bright and within the probed 350-650 nm spectral range) from the $^3\pi\pi^*$ $^3n\pi^*$ states, eventually populated after inter-system crossing out of the singlet $^1n\pi^*$ state. These spectral densities were used to simulate the fingerprint excited state absorption signal of the triplet manifold around 525 nm (600 nm in the experiment, see Figures 1B and 1D). The spectral densities were constructed using the same procedure outlined for obtaining

the spectral density of the lowest singlet $^1\pi\pi^*$ state. Thereby, the electronic structure of the manifold of higher lying excited states was computed at the $^3\pi\pi^*$ and $^3n\pi^*$ minima at the SS-CASPT2/SA-6-CASSCF(16,12) level of theory (orbitals given in Figure S6) and gradients were calculated for the roots with considerable oscillator strength. Two roots (root 4 and root 5) were considered for $^3\pi\pi^*$, one root (root 4) was considered for $^3n\pi^*$. The spectral densities are constructed using displacements $\tilde{\boldsymbol{d}}_f$ relative to the corresponding minimum. All coefficients are listed in Table S2. Furthermore, through state-averaging of up to 15 roots it was assured that there are no further bright excited states that fall within the probed spectral window.

1.3.6 Parameters for the overdamped Brownian oscillator (OBO) model

The parameters for the OBO model (eq. 17) were chosen so to reproduce the bandwidth of the linear absorption spectrum at room temperature where inhomogeneous broadening contribution was neglected. Best fit was obtained for coupling strength $\lambda = 400$ cm^{-1} and time scale $\Lambda = 1/50$ fs^{-1}. For simplification, the same OBO parameters were used for all states.

1.3.7 Accounting for realistic pulses

Finite pulse duration is accounted for ad-hoc by convoluting the PP signal $W^{(3)}(t_2, \Omega_3)$ with a Gaussian function in the time domain

$$W^{(3)}(t_2, \Omega_3) = \int_{-\infty}^{+\infty} d\tau \; W^{(3)}(\tau, \Omega_3) \; \exp\left(-\frac{(\tau - t_2)^2}{2\sigma^2}\right) \tag{29}$$

A standard deviation $\sigma = 8 \; fs$ was used (matching the experimental full-width-half-maximum of 16 fs).

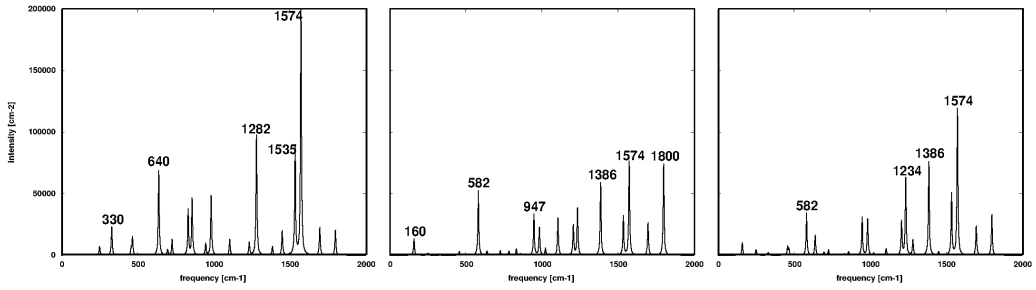

Figure S5: Spectral densities of the higher lying excited states accessible from the triplet states $^3\pi\pi^*$ (left and middle) and $^3n\pi^*$ (right). See also Table S2.

2 Simulation results

2.1 Electronic structure at representative geometries

Figure S6 summarizes the electronic structure of 4-thiouracil in aqueous solution. The lowest $\pi\pi^*$ transition is $\pi_S \rightarrow \pi_1^*$ at 3.73 eV (332 nm) with an oscillator strength 0.43 at the SS-CASPT2/SA-4-CASSCF(16,12) level, followed by $\pi_2 \rightarrow \pi_1^*$ absorbing at 4.39 eV (282 nm), exhibiting oscillator strength of 0.04. One $n\pi^*$ transition involving the sulfur lone pair appear in the window above 300 nm, the $n_S \rightarrow \pi_1^*$ absorbing at 2.82 eV (400 nm). This transition is essentially dark. We note the large $n_S \rightarrow \pi_1^*/\pi_S \rightarrow \pi_1^*$ gap of 0.90 eV.

	state	electr. trans. (weight)	E [eV]	o.s.	orbitals
Min S_0	S_0	GS (0.88)	0.00		
	S_1	n_S-π_1* (0.88)	2.82	0.00	
	S_2	π_S-π_1*(0.73)	3.73	0.43	
	S_3	π_2-π_1*(0.64)	4.39	0.04	
Min nπ*	S_0	GS (0.84)	0.30		
	S_1	n_S-π_1* (0.87)	2.58	0.00	
	S_2	π_S-π_1*(0.74)	3.56	0.35	
	T_1	π_S-π_1*(0.31) n_S-π_1* (0.34)	2.46		
	T_2	n_S-π_1* (0.45) π_S-π_1*(0.34)	2.56		
Min ππ*	S_0	GS (0.84)	0.35		
	S_1	n_S-π_1* (0.86)	2.73	0.00	
	S_2	π_S-π_1*(0.74)	3.47	0.33	
	S_3	π_2-π_1*(0.69)	4.40	0.11	
CI nπ*/ππ*	S_1	n_S-π_1* (0.87)	3.42		
	S_2	π_S-π_1*(0.62)	3.67		
Min ππ*$_{S3}$	S_2	π_S-π_1*(0.72)	3.52	0.31	
	S_3	π_2-π_1*(0.66)	4.38	0.10	
CI ππ*/ππ*$_{S3}$	S_2	π_S-π_1*(0.71)	4.41		
	S_3	π_2-π_1*(0.77)	4.38		
Min ^{3}ππ*	S_0	GS(0.83)	0.23		
	S_1	n_S-π_1* (0.83)	2.61		
	T_1	π_S-π_1*(0.61)	2.35		
	T_2	n_S-π_1* (0.73)	2.68		
Min ^{3}nπ*	S_0	GS(0.83)	0.24		
	S_1	n_S-π_1* (0.88)	2.58		
	T_1	π_S-π_1*(0.74)	2.45		
	T_2	n_S-π_1* (0.87)	2.57		

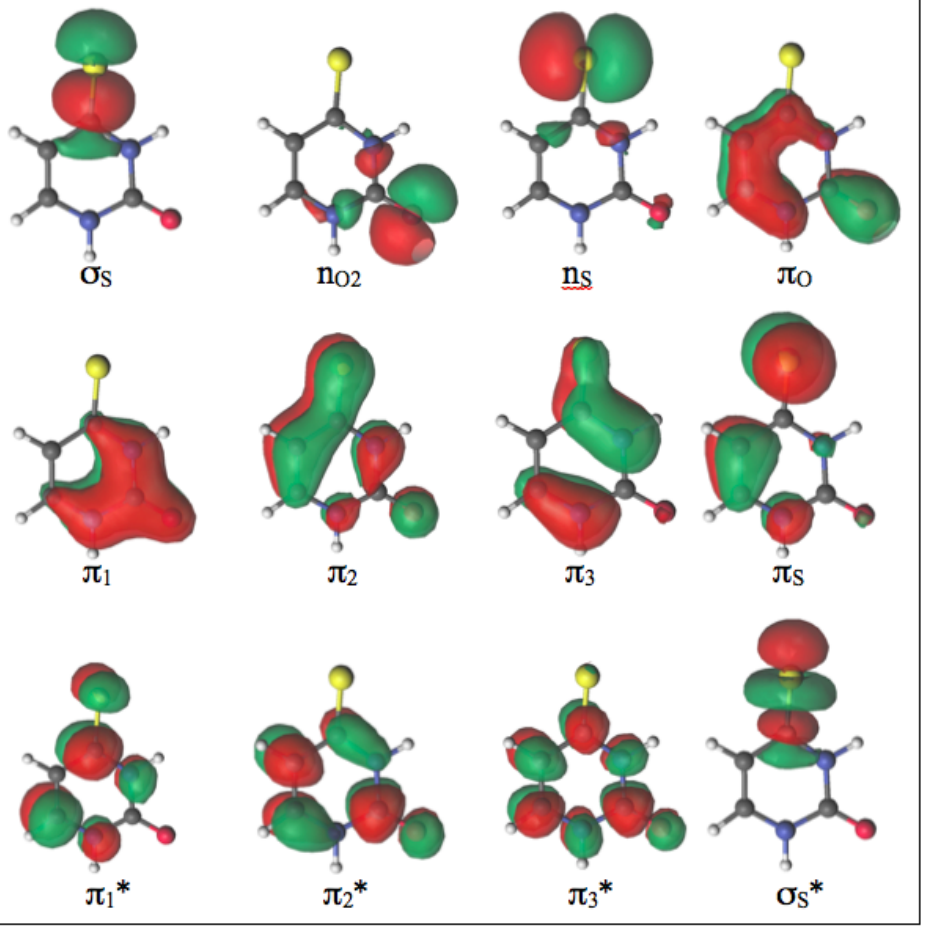

Figure S6: Vertical transition energies (E), oscillator strength (o.s.), leading configuration state functions (CSF) and the associated weights (in brackets) of the lowest singlet and triplet states at all critical points of 4-thiouracil obtained at the SS-CASPT2/SA-CASSCF(16,12) level. Active space orbitals shown to the right.

2.2 Linear absorption spectrum

Figure S7 left panel shows the LA spectra of 4-thiouracil obtained by semi-classical sampling at room temperature at the SS-CASPT2 level of theory. A minimal full valence-π CAS(10,8) (red line), as well as two active spaces augmented by four and eight extra-valence virtual orbitals, denoted as RAS$(10,8|2,4)$ (green line) and RAS$(10,8|2,8)$ (blue line) are compared to the experimental spectrum (black line). The LA spectrum above 230 nm is characterized by an intense band peaking at 330 nm and a weak band around 250 nm. At the SS-CASPT2 level we notice that the minimal CAS(10,8) red-shifts the absorption band by ca. 20 nm ($\sim$ 0.20 eV at this wavelength). The addition of four and eight virtual orbitals corrects the red-shift to give an excellent agreement with the experimental absorption maximum. However, we note that the simulated spectrum decay smoother at long wavelengths compared to the experiment. Instead, and quite remarkably, the LA spectrum constructed by means of cumulant expansion of Gaussian fluctuations (ocher, see sec. 1.3.1) with line shape functions (sec. 1.3.4) within the DHO model normal mode analysis (sec. 1.3.3) reproduces quantitatively the LA spectrum. Due to the involvement of low frequency mode (457 cm^{-1}, 697 cm^{-1} and 783 cm^{-1}) with large Huang-Rhys factors the spectrum shows no fine vibrational structure (even at low temperature) and exhibits a weak dependence on the system-bath coupling strength and fluctuation time scale (eq. 17).

Next, we focus on the individual contributions to the spectrum. To this aim we expand the RAS$(10,8|2,4)$, shown above to produce spectra in excellent agreement with the experimental data, by including the sulfur lone pair thus obtaining a RAS$(12,9|2,4)$ capable of resolving the relative positions of the bright and dark bands. Figure S7 right panel demonstrates that the inclusion of the lone pair introduces a 5 nm red-shift in the SS-CASPT2 spectrum (compare solid (RAS$(12,9|2,4)$) and dotted (RAS$(10,8|2,4)$ red lines). The lowest absorption band emerges exclusively due to the $\pi_S \rightarrow \pi_1^*$ transition (purple). The weak band around 250 nm has contributions from two transitions, $\pi_2 \rightarrow \pi_1^*$ (brown) and $\pi_S \rightarrow \pi_2^*$ (cyan). The lowest $n\pi^*$ transition $n_S \rightarrow \pi_1^*$ in the system is found to overlap with red part of the $\pi_S \rightarrow \pi_1^*$ band, despite the 0.90 eV energy gap between both transitions at the equilibrium geometry (Table in Figure S6). The accurate prediction of the spectral position is important for the correct selection of samples for the MD simulations. As seen in Figure S7 left panel, if one would rely on a full π-valence AS for the simulations (red line in Figure S7, left) and would select snapshots between 320-340 nm (under the envelope of the experimental pump pulse shown in brown in Figure S7, left) belonging to the high energy

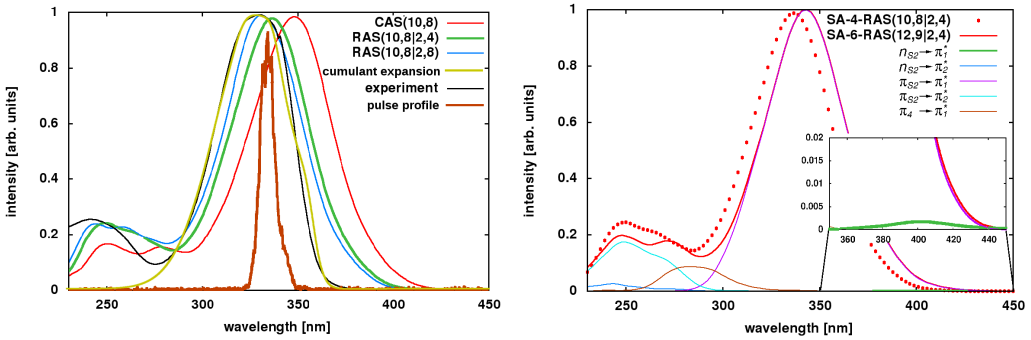

Figure S7: Left: Dependence of the LA spectrum of 4-thiouracil on the size of the active space size. Experimental spectrum in aqueous solution given as reference in black. Profile of the experimental pump pulse shown in brown. LA spectrum obtained with the CGF method (sec. 1.3.1) with line shape functions (sec. 1.3.4) constructed within the DHO model normal mode analysis (sec. 1.3.3) shown in ocher. Right: Decomposition of the LA spectrum, obtained at the SS-RASPT2/SA-6-RASSCF(12,9—2,4) level into contributions from individual transitions.

region of the $\pi\pi^*$-band. Instead, in reality, the pump pulse excites the center of the band.

2.3 Trajectory plots

Figures S9-S12 show the evolution of the energies of the ground state (black), first excited (S_1, red), second excited (S_2, green) and photoactive (cyan) sates, as well as the total and kinetic energy (cyan) along the 30 trajectories run in the course of this work. All trajectories were initiated in S_2 which at the Franck-Condon point is of $\pi\pi^*$ nature and were run for up to 180 fs. Remarkably, despite the 1 eV energy gap at the equilibrium geometry the sampling of vibrational degrees of freedom decreases this energy considerably (see Figure S8). Thus, while at equilibrium the energy gap is 1 eV, in the spectral region [330:355nm] addressed by the pump pulse the average S_2/S_1 energy gap is about 0.5 eV.

In trajectories 4, 5, 6, 8, 10, 11, 14, 19, 20, 21, 24, 29, 30 the internal conversion occurs within 20 to 40 fs, i.e. within one to two C−5-C_6 oscillations. Few trajectories remaining on S_2 until the end of the simulation (15, 17, 25). In contrast to 2-thiouracil, whose dynamics was recently studied in gas-phase [Mai16], we do not observe sulfur-out-of-plane deformation in the $n\pi^*$ state. Instead, the system tends to preserve planarity. Furthermore, we noticed that, $n\pi^* \rightarrow \pi\pi^*$ re-crossings do not occur once the population is

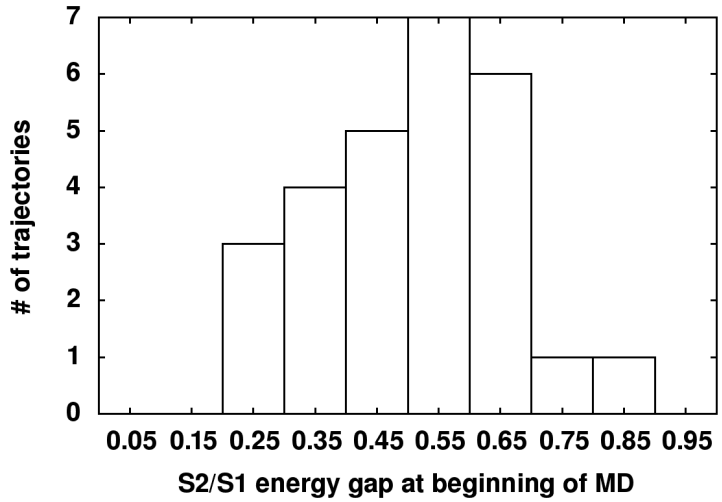

Figure S8: Distribution of S_2/S_1 energy gaps at the beginning of the MD simulations

entirely in the state with $n\pi^*$ configuration. We also do not observe hops to the ground state, the $GS - n\pi^*$ gap being in the range of 50 kcal/mol and never decreasing below 20 kcal/mol. The $GS - n\pi^*$ gap decrease is favored by hydrogen-out-of-plane deformations.

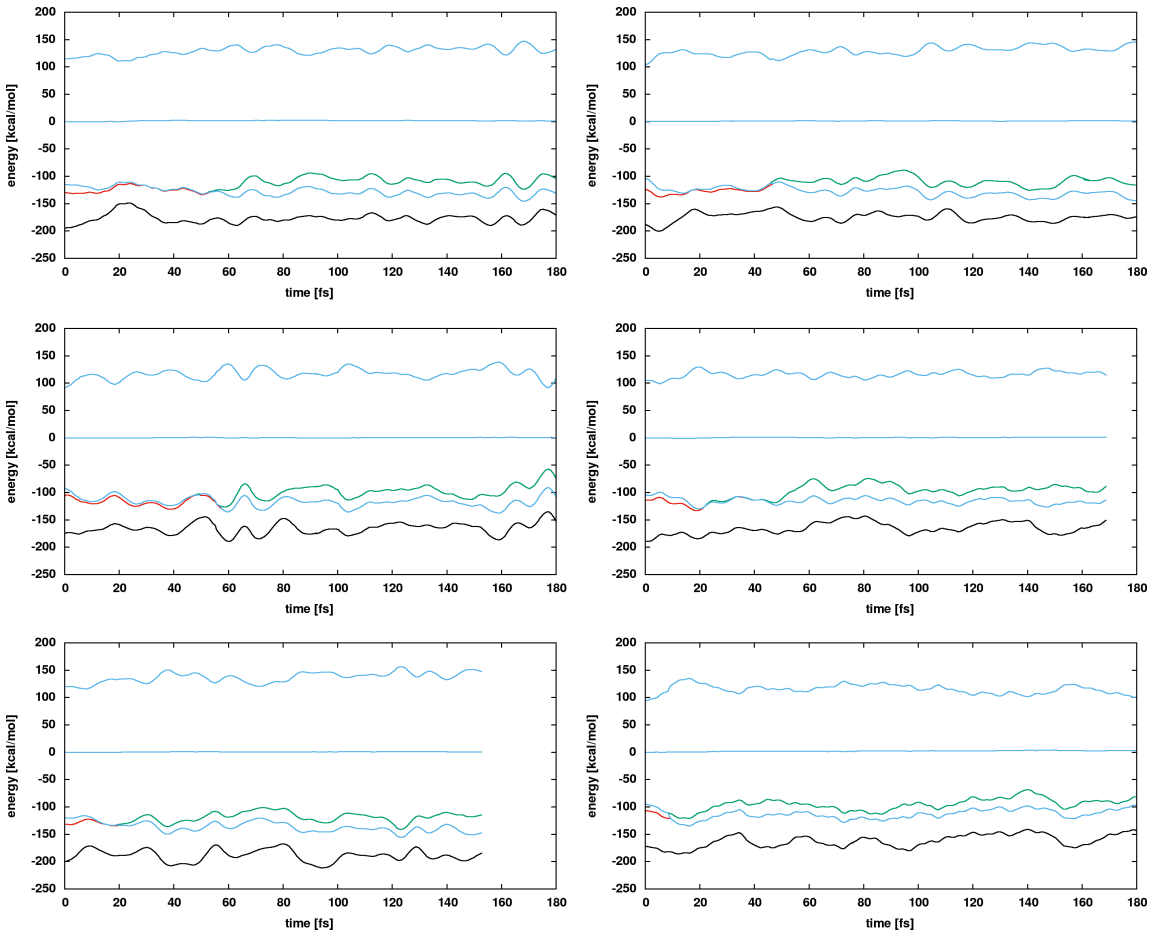

Figure S9: Trajectories 1-6. Legend: GS (black), $n\pi^*$ (red), $\pi\pi^*$ (green), photoactive state (cyan), total energy (cyan), kinetic energy (cyan).

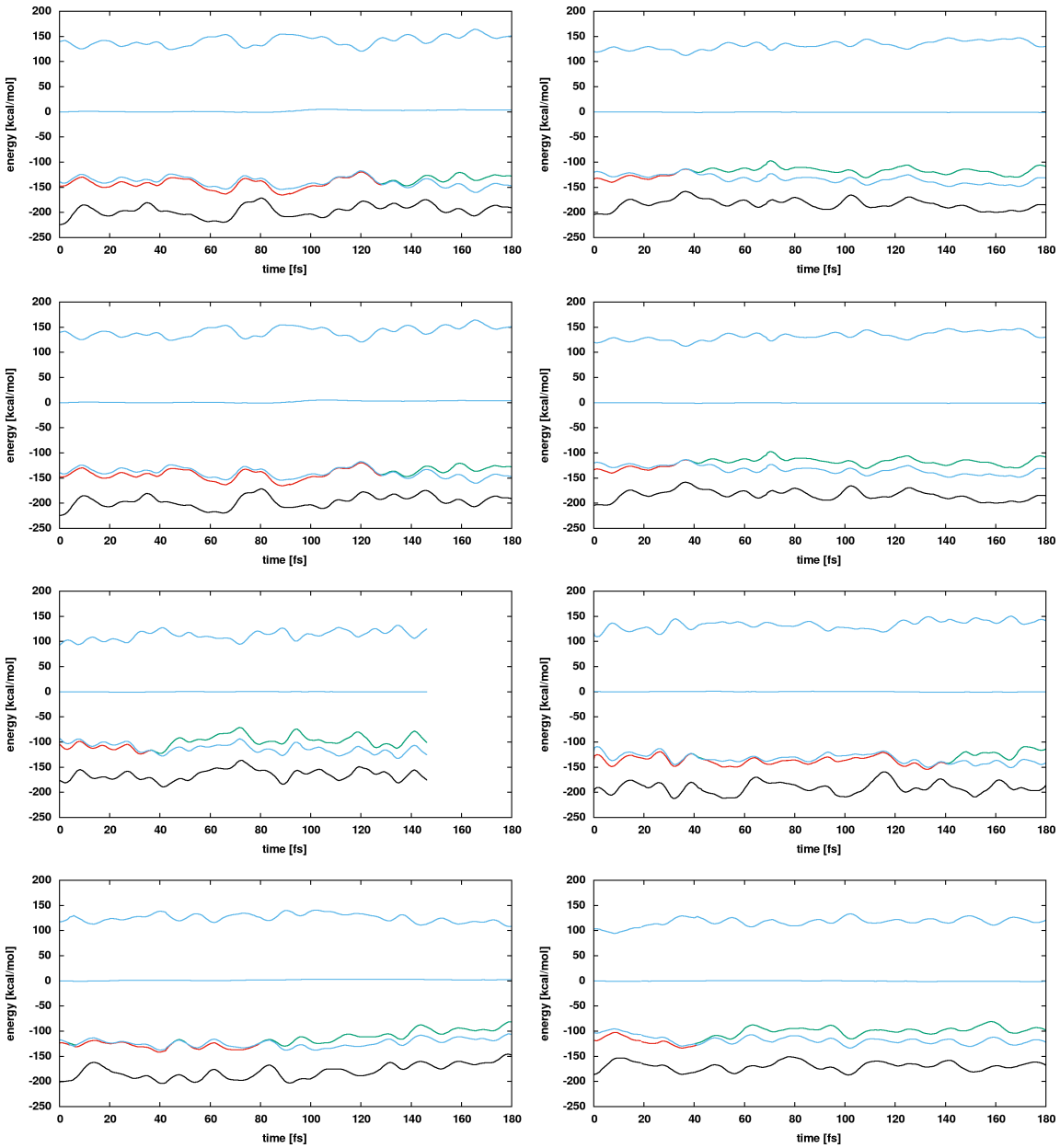

Figure S10: Trajectories 7-14. Legend: GS (black), $n\pi^*$ (red), $\pi\pi^*$ (green), photoactive state (cyan), total energy (cyan), kinetic energy (cyan).

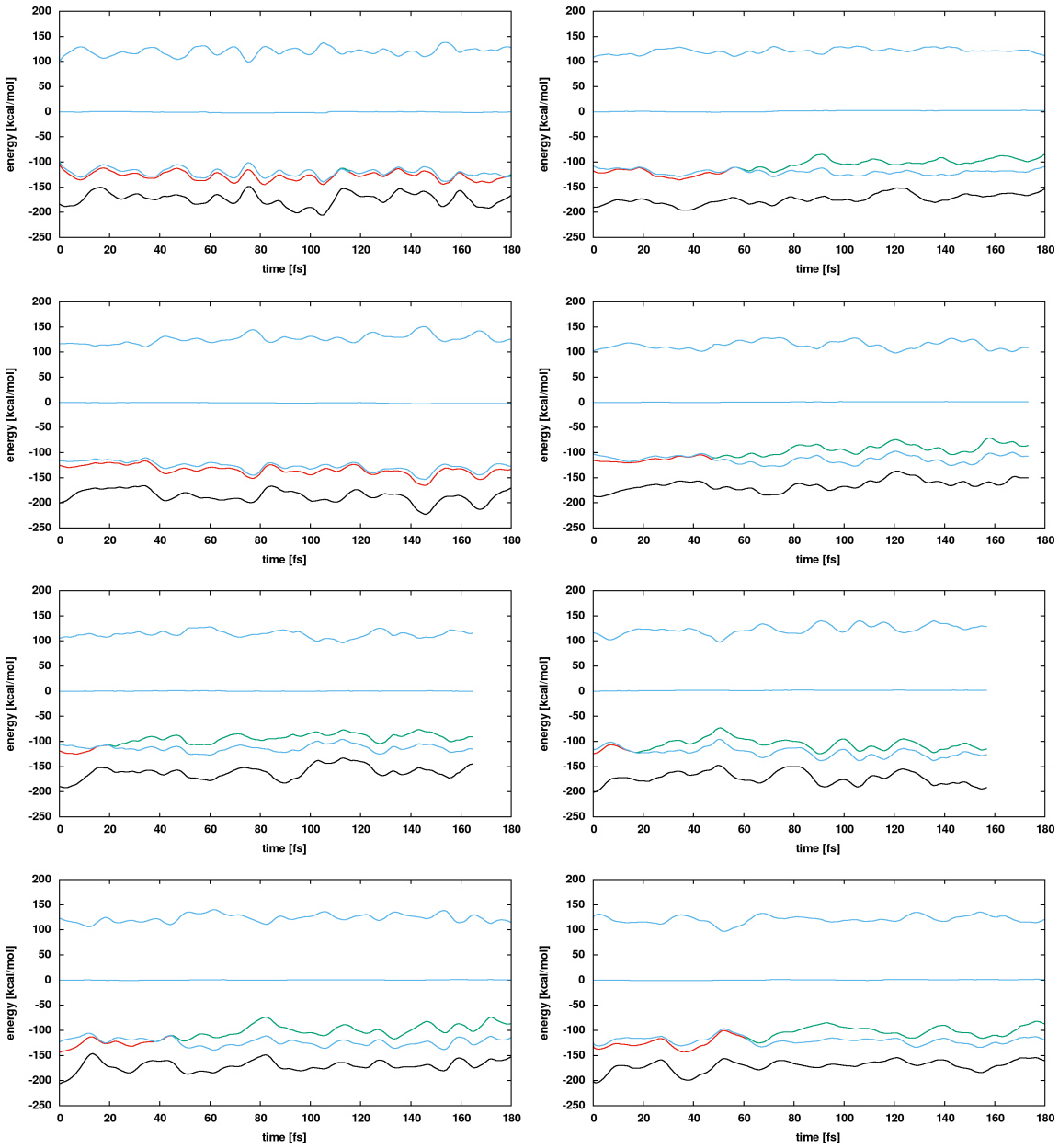

Figure S11: Trajectories 15-22. Legend: GS (black), $n\pi^*$ (red), $\pi\pi^*$ (green), photoactive state (cyan), total energy (cyan), kinetic energy (cyan).

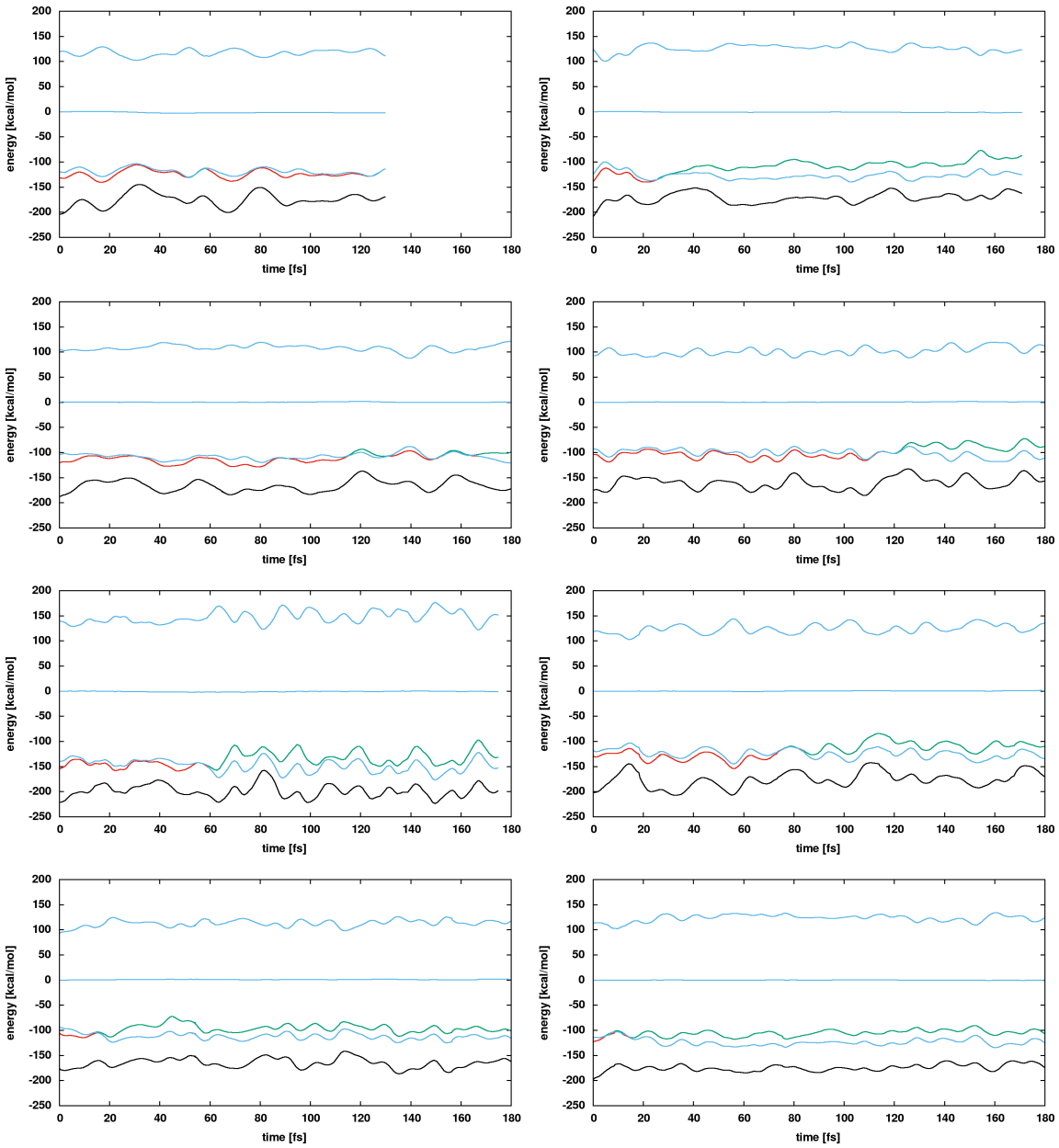

Figure S12: Trajectories 23-30. Legend: GS (black), $n\pi^*$ (red), $\pi\pi^*$ (green), photoactive state (cyan), total energy (cyan), kinetic energy (cyan).

2.4 Population dynamics

The population of the second excited state $\overline{a}_{S_2}(t)$ (quantum mechanical quantity), shown in blue in Figure S13, was computed as follows:

$$\overline{a}_{S_2}(t) = \frac{\sum_j \left|c_j(t)\right|^2}{N_{\text{tot}}} \tag{30}$$

The fraction of trajectories $N_{S_2}(t)$ in the second excited state (classical quantity), shown in red in Figure S13, was computed as follows:

$$f_{S_2}(t) = \frac{N_{S_2}(t)}{N_{\text{tot}}}. \tag{31}$$

It is the state with $\pi\pi^*$ configuration (diabatic picture) and not always the adiabatic S_2 that is the source of the stimulated emission, whose ultrafast decay in turn is used to extract the lifetime of the bright state. It has to be considered that for certain geometrical deformations the energetic order of $\pi\pi^*$ and $n\pi^*$ might change, i.e. the $\pi\pi^*$ state might become the lowest excited state. Thus, a second classical quantity, the fraction of trajectories $N_{\pi\pi^*}(t)$ in the state with $\pi\pi^*$ configuration, shown in green in Figure S13, was computed following eq. 31, whereas the number of trajectories in the state with $\pi\pi^*$ configuration was obtained by exploiting the large difference the magnitude of the transition dipole moments of $\pi\pi^*$ and $n\pi^*$. The temporal profile of the fraction $f_{\pi\pi^*}(t)$ was fitted with a mono-exponential function of the form $e^{-t/t_{\pi\pi^*}}$ in order to obtain the lifetime of the bright state. The fit is shown in black in Figure S13.

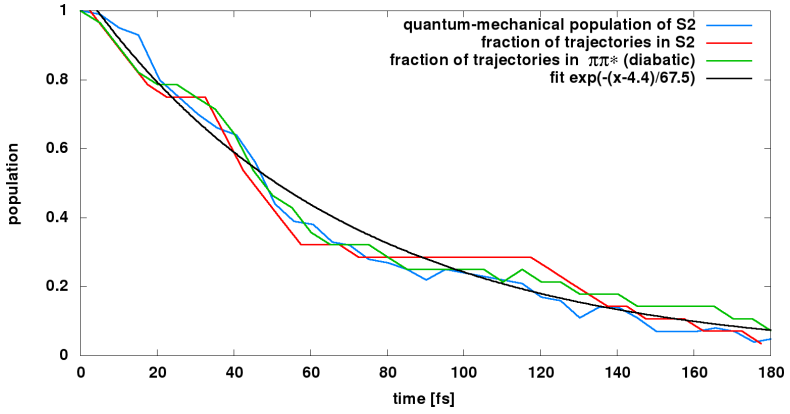

Figure S13: Legend: GS (black), $n\pi^*$ (red), $\pi\pi^*$ (green), photoactive state (cyan), total energy (cyan), kinetic energy (cyan).

2.5 Normal mode analysis

In this section we analyze the trajectories for coherent vibrational features. To this aim we projected the geometrical deformations along each trajectory (i.e. the difference in Cartesian coordinates between the geometry at time t and the ground state equilibrium geometry) on the ground state normal modes (thus neglecting Duschinsky rotations). In particular, we used eq. 28 with a time-dependent difference $\Delta\boldsymbol{Q}(t)$ in the Cartesian coordinate space

$$\boldsymbol{q_i}(t) = \mathbb{P}^{-1}\mathbb{M}^{\frac{1}{2}}\Delta\boldsymbol{Q}(t) \tag{32}$$

to obtain time-dependent displacement vector $\boldsymbol{q_i}(t)$ containing the displacements q_{ik} along each normal mode $\boldsymbol{\xi}_k$. With $\boldsymbol{q_i}(t)$ at hand we are able to decompose the expression for the energy gap 23 and show the oscillatory dynamics $\Delta E_{ijk}(\tilde{\boldsymbol{q}}(t))$ along each mode $\boldsymbol{\xi}_k$.

$$\Delta E_{ijk}(\tilde{q_k}(t)) = \frac{1}{2}\omega_k^2\tilde{d}_{ik}^2 - \omega_k^2\tilde{d}_{ik}\tilde{q}_{ik}(t), \tag{33}$$

with $i \in \{^1\pi\pi^*, ^1 n\pi^*\}$. Thereby, when evaluating eq. 33, either the excited state equilibrium displacements $\tilde{d}_{\pi\pi^*,k}$ or $\tilde{d}_{n\pi^*k}$ (with respect to the ground state, sec. 1.3.4 and Table S1) are considered, depending on the state in which the dynamics is evolving. For several modes we resolve coherent vibrations which lead to a significant modulation of the energy gap (see Figures S14 and S15). We map them to the same normal modes dominating the spectral density (see Figure S4). However, as the dynamics simulations is run in the excited state the oscillation period differs slightly from the one in the ground state. For example, the ring breathing dynamics, which has an oscillation period of 73 fs in the ground state, corresponding to a frequency of 457 cm^{-1}) and thus in agreement with Raman data (440 cm^{-1}), is found to have a period of $\sim$ 90 fs in the excited state, which corresponds to a frequency of 370 cm^{-1}, which in turn matches the 400 cm^{-1} mode obtained from the PP spectra analysis. Two modes with ground state frequencies of 697 cm^{-1} and 784 cm^{-1} are responsible for the spectral dynamics with a 680 cm^{-1} frequency. It should be noted that in the excited state the two modes exhibit frequencies of 710 cm^{-1}) and 665 cm^{-1}, respectively. They both describe hydrogen out-of-plane deformations.

In the mid- and high-frequency window we encounter further coherent oscillations associated associated with hydrogen in-plane bending and with bond stretchings. In particular, coherence is retained most clearly for the N_2-C_3 and C_3-C_4 stretchings. The C_3-C_4 stretching exhibits the most pronounced modulation of the energy gap at early times (ca. 10 kcm^{-1}), related to the large displacement $\tilde{\boldsymbol{d}}_{\pi\pi^*,25}$ of 0.28 $Bohr\sqrt{amu}$ (Table S1). Both modes

shows slightly prolonged oscillation periods ($\sim 22-23$ fs) with respect to the ground state ($\sim$ 20 fs), probably due to the reduced double bond character in the excited state.

After decay to the $S_1(^1n\pi^*)$ state through the CI($^1\pi\pi^*/^1n\pi^*$) the excess energy, initially accumulated in eight modes dominating the spectral density of the S_2 state (Figure S4) and shown in Figures S14 and S15) remains mostly stored in the same vibrational modes after transfer to the $^1n\pi^*$ state. This is recognized by looking at the coherent oscillations of the relative displacements q_{ik} for each mode k with respect to the GS equilibrium geometry along the dynamics (i.e. large values of q_{ik} indicate strong deformation along the k-th mode). We observe coherent oscillations along the breathing mode (457 cm^{-1}, Figure S16A) shows the hydrogen out-of-plane bending modes (697 cm^{-1} and 784 cm^{-1} and the mid frequency hydrogen in-plane bending mode (1106 cm^{-1}, 1207 cm^{-1} and 1234 cm^{-1}, Figure S16B), during the entire duration of the molecular dynamics (i.e. up to 180 fs). Unlike the stimulated emission signal, which decays on a sub-100 fs time scale the vibrational coherences do not disappear once the population is in the $^1n\pi^*$ state as energy redistribution takes longer than 200 fs. On the other hand, the high frequency stretching modes (1574 cm^{-1} and 1698 cm^{-1}, Figure S16C) exhibit a faster damping and toward the end of the simulation show oscillations with weak amplitude.

Interestingly, we observe the activation of low frequency out-of-plane modes (70 cm^{-1} and 160 cm^{-1}, Figure S16D) which break the ring planarity by moving either N_1 or N_3 out-of-plane (by up to 20°) and distorting also the adjacent hydrogen thus inducing a characteristic puckering. We remind that the 70 cm^{-1} mode was excluded in the sampling as we observed breaking of the quadratic approximation and sampling of strongly distorted geometries. Yet, we find out that energy redistribution in this mode sets up within ca. 60 fs.

2.6 Planar and twisted regions of the S_2 PES

Recently, Martínez-Fernández at al. reported a joint experimental / theoretical study on the closely related 5-methyl-4-thiouracil (4-thiothymine). The pump (at 270 nm, 334 nm and 387 nm) - probe (400-700 nm range) spectra with 200 fs temporal resolution were supplemented with potential energy surface exploration at the CASSCF level (augmented with CASPT2 correction at optimized geometries for accurate energetics) and semi-empirical (FOMO-CI) molecular dynamics simulations covering 10 ps after excitation with the pump pulse [Mar17]. Ring twisting is found to be essential for the $^\pi\pi^*$ state decay. The authors report a twisted minimum S_{2T} which promotes the decay

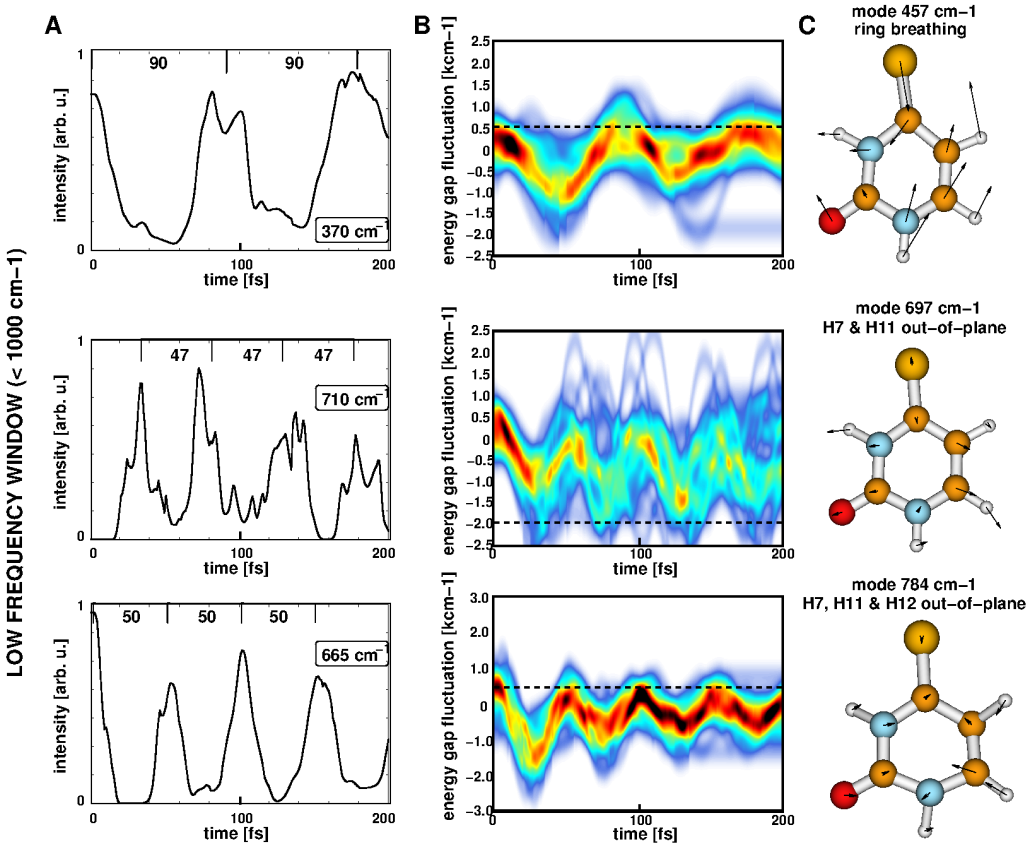

Figure S14: Decomposition of the excited state dynamics in the contributions of the individual active modes. Shown are energy gap fluctuations for the dominant modes with large displacements $\tilde{d}_{ik}$ in the frequency range below 1000 cm^{-1}.

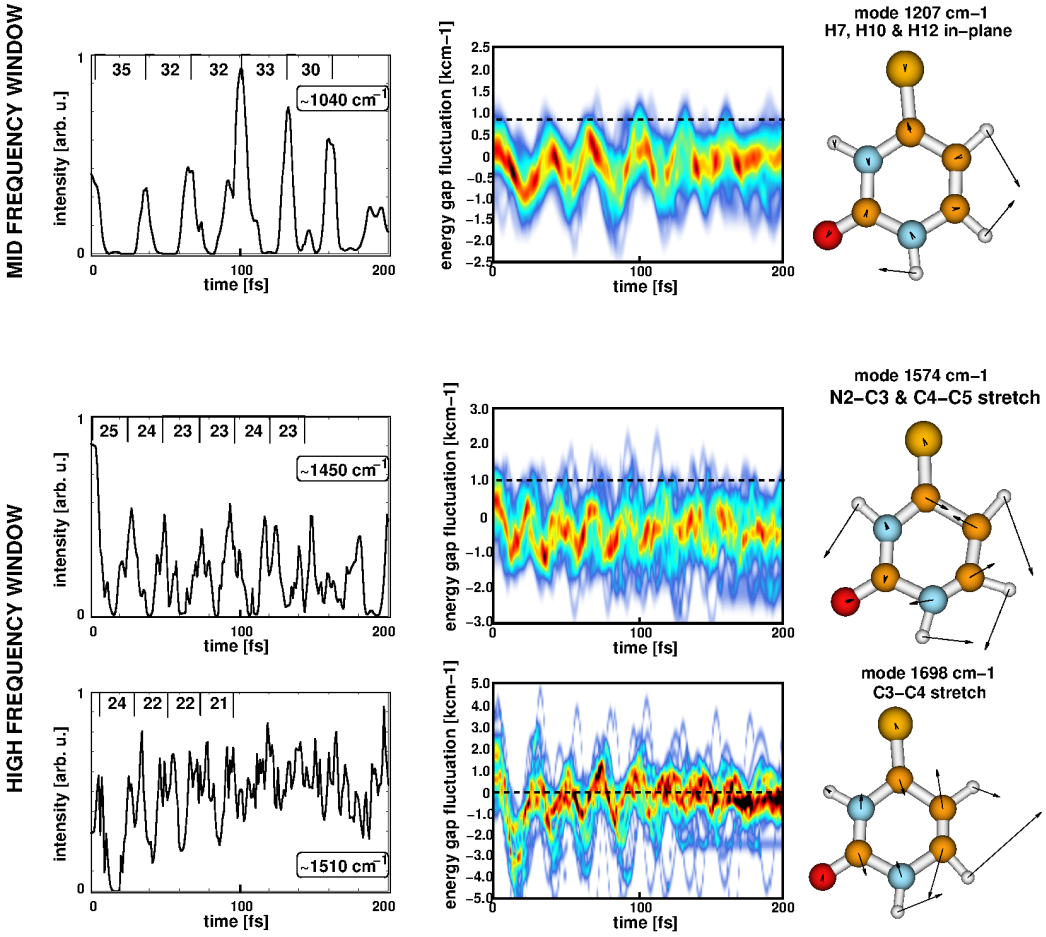

Figure S15: Decomposition of the excited state dynamics in the contributions of the individual active modes. Shown are energy gap fluctuations for the dominant modes with large displacements $\tilde{d}_{ik}$ in the frequency range above 1000 cm^{-1}.

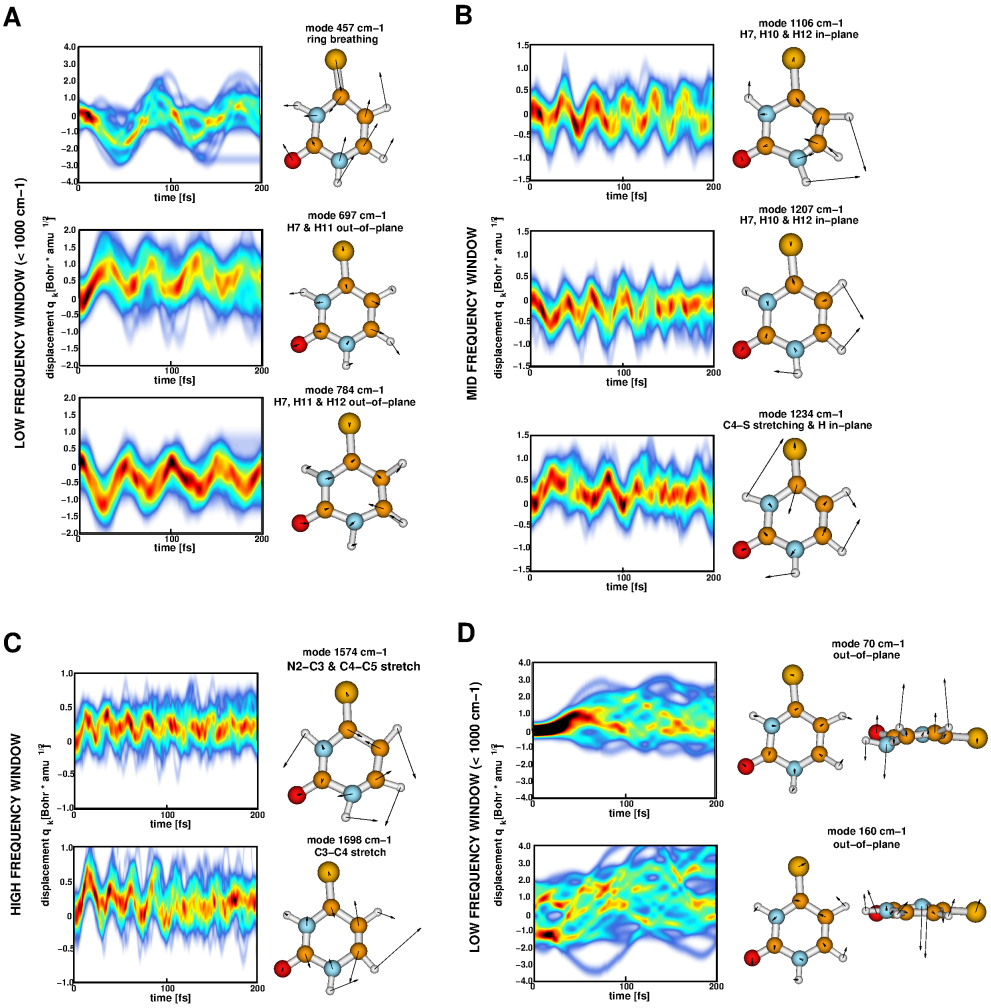

Figure S16: Fluctuation of the relative displacement q_{ik} with respect to the GS equilibrium along selected vibrational modes.

with a 1.0 ps time constant, while the planar minimum S_{2P} is found to trap part of the population which decays with 3.6 ps.

Starting from a geometry distorted in a way similar to the structure of S_{2T} shown in Figure 1 of ref. [Mar17] we were able to locate an out-of-plane conformation (see Figure S17) for 4-thiouracil. The minimum was located at the MS-5-CASPT2/CASSCF(12,9)/ANO-L with contraction for C and N [4s3p2d], for H [3s2p1d] and for S [5s4p3d2f] by minimizing the energy of the third state. The geometry of S_{2T} is characterized with a slightly distorted ring planarity most suitably described by dihedrals $C_2N_3C_4C_5 = 30°$, $N_3C_4C_5C_6 =$ -33°and $C_2N_3C_4S = 197°$. Furthermore, we note the strongly elongate C4C5 bond (1.47 Å at S_{2T} vs. 1.38 Å at S_{2P}). As also reported in [Mar17] this minimum is higher in energy compared to the planar minimum. Figure S17 depicts the energetics of the FC point and both minima on the S_2 PES. Linear interpolation between the points provides an idea about the PES profile. It attracts attention that the twisted minimum is of the same energy as the FC point, i.e. 0.35 eV above the planar minimum. Furthermore, we note the negligible barrier connecting S_{2T} to S_{2P}. This makes S_{2T} meta-stable, but we do not exclude the possibility that it is an artifact of the method used. The twisted minimum is characterized by a slightly smaller ${}^1\pi\pi^*/{}^1n\pi^*$ energy gap of 0.37 eV compared to 0.56 eV at S_{2P}. Contrary to what is reported for 4-thiothymine in [Mar17] the conical intersection we find between ${}^1\pi\pi^*/{}^1n\pi^*$ is planar (thus geometrically closer to S_{2P}) and energetically 0.2 eV above S_{2P} (thus below S_{2T}). The emission spectrum of the twisted geometry peaks at 382 nm (S0-S1 energy gap at S_{2T} is 3.25 eV).

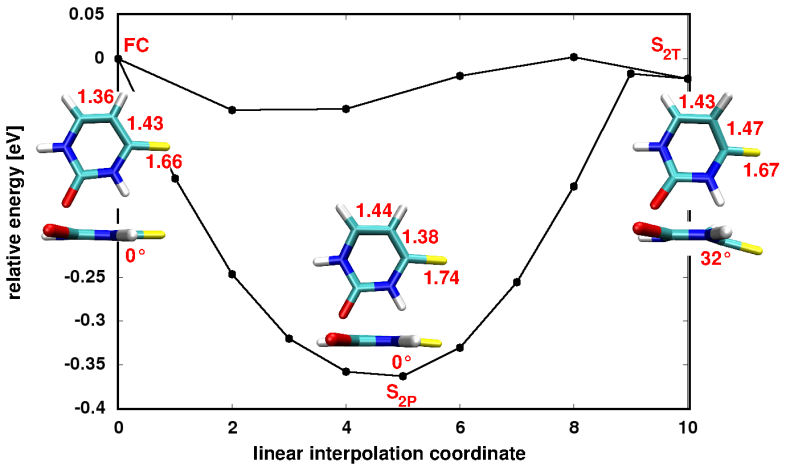

Figure S17: Linear interpolation between FC and both minima - planar (P) and twisted (T) - on the PES of the $S_2(^1\pi\pi^*)$ state. Characteristic coordinates are given.

We analyzed the trajectories focusing on the in-plane (bond stretching) and out-of-plane (ring puckering, sulfur pyramidalization) dynamics in the system (Figure S18). From the plots of the $N_3C_4C_5C_6$ (-33°at S_{2T}), $C_2N_3C_4C_5$ (30°at S_{2T}) and $C_2N_3C_4S$ (197°at S_{2T}) dihedrals it is evident that 4-thiouracil explores the region of near-planarity and does not reach values of 30°out-of-plane deformation. Furthermore, we note that the bond lengths exhibit oscillations with large amplitudes in the first 100 fs. The C_5-C_6 and C_4-S exhibit pronounced elongation from 1.36 Å and 1.65 Å to 1.52 Å and 1.90 Å, respectively, while the C_4-C_5 bond is shortened from 1.43 Å to 1.34 Å. These initial deformations which determine the first 20 fs of the S_2 dynamics correspond to the deformations required to reach S_{2P}. Thus, as expected from the linear interpolation (Figure S17) the system exhibits initially a strong gradient toward S_{2P}. No out-of-plane motion is activated in the FC region. After the initial large oscillation amplitude the C_4-C_5 bond is damped to $1.38 - 1.42$ Å, while the C_4-S bond shortens gradually in the next 80 fs to 1.7 Å.

Next, we analyzed the geometries of the hopping events along the 30 trajectories. Thereby, we limited the analysis to 47 hopping events (some trajectories exhibit more than one hopping event in the course of the simulation) at which the $^1\pi\pi^*/^1n\pi^*$ energy gap is less than 0.01 eV which can be regarded as a conical intersection. The results are presented in Figure S19. The conical intersections are characterized with significantly elongated C_5-C_6 and C_4-S bond lengths and with a shortened C_4-C_5 bond length, with values well beyond S_{2P} equilibrium. The elongation of the C_5-C_6 bond was found

in the PES exploration to be essential for reaching the conical intersection. The hopping occurs at slightly distorted geometries showing predominantly negative deformation of the $N_3C_4C_5C_6$ dihedral and predominantly positive deformation of the $C_2N_3C_4C_5$. The same trend is encountered at S_{2T} which suggests that the conical intersection seam lies in the same direction (relative to S_{2P}) as the twisted minimum. Finally, the sulfur is found to fluctuate $\pm 10°$above the plane of the ring.

Based on the above analysis we are confident that, albeit present, the twisted minimum S_{2P} on the PES of the $^1\pi\pi^*$ state is not involved in the deactivation dynamics.

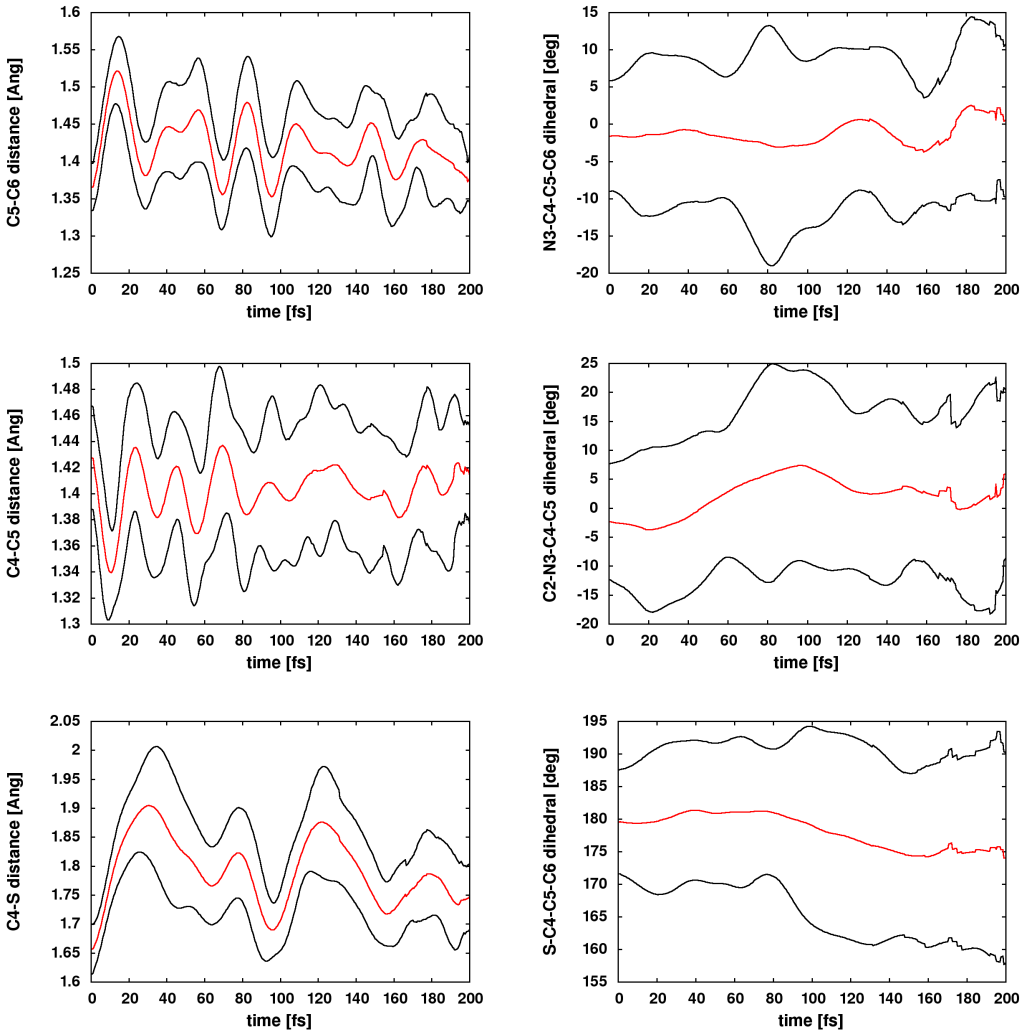

Figure S18: Evolution of several representative coordinates averaged over 30 trajectories (red) with standard deviation (black).

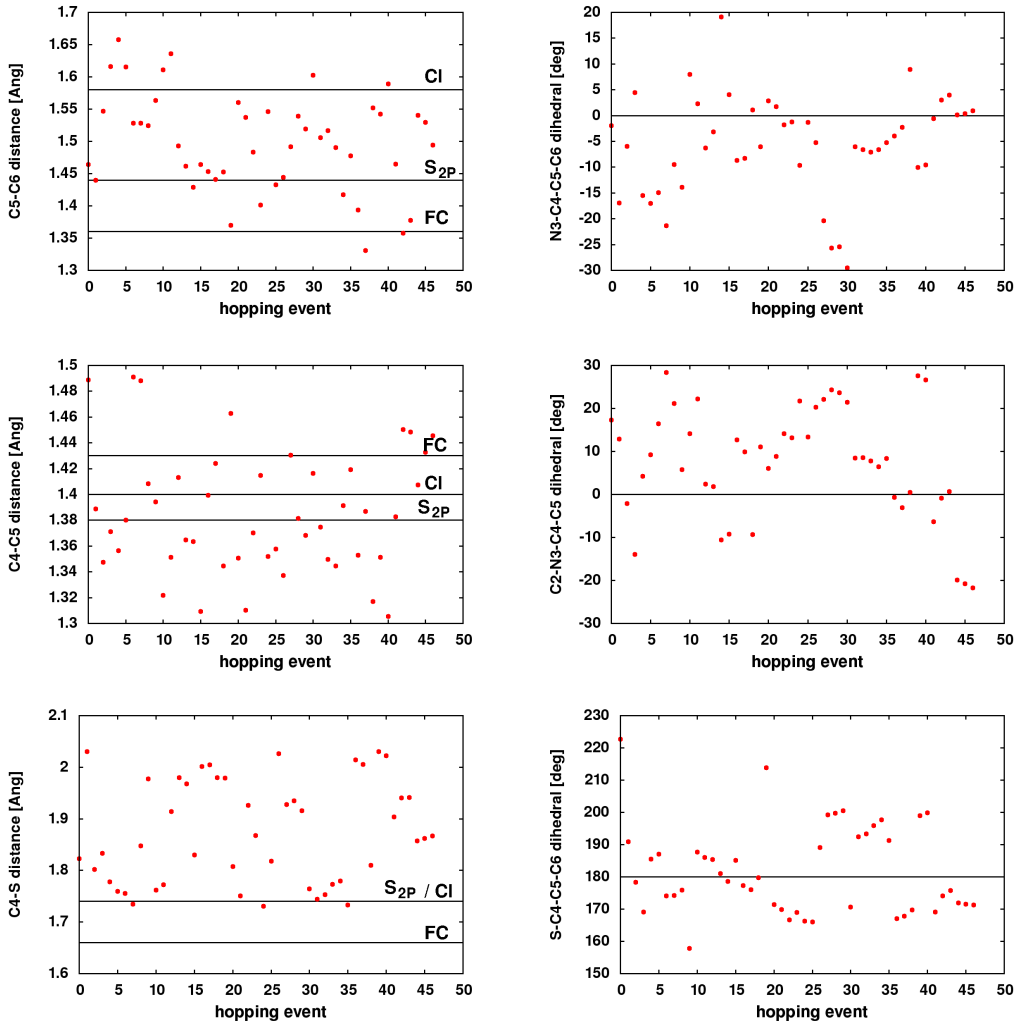

Figure S19: Values for several important coordinates at the hopping events. 47 structures were selected out of the 30 MD simulations with $^1\pi\pi^*/^1n\pi^*$ energy gap of 0.1 eV.

2.7 Parameters for the DHO model

Table S1. Parameters for constructing the spectral densities of the singlet states $^1\pi\pi^*$ and $^1n\pi^*$ based on the normal mode analysis method (sec. 1.3.3). The parameters of the $^1\pi\pi^*$ are used to simulate the linear absorption spectrum and the stimulated emission in the pump probe spectra.

Normal mode		$^1\pi\pi^*$		$^1n\pi^*$	
№	ω [cm^{-1}]	ε_e^a [cm^{-1}]	28600^b	ε_e^a [cm^{-1}]	20800
ω_2	160	$\tilde{d}_2$	0.34	$\tilde{d}_2$	0.39
ω_3	251	$\tilde{d}_3$	0.16	$\tilde{d}_3$	0.33
ω_4	330	$\tilde{d}_4$	0.19	$\tilde{d}_4$	0.22
ω_5	457	$\tilde{d}_5$	0.42	$\tilde{d}_5$	0.27
ω_6	467	$\tilde{d}_6$	0.09	$\tilde{d}_6$	0.05
ω_7	583	$\tilde{d}_7$	0.18	$\tilde{d}_7$	0.01
ω_8	640	$\tilde{d}_8$	0.06	$\tilde{d}_8$	0.03
ω_9	698	$\tilde{d}_9$	0.29	$\tilde{d}_9$	0.42
ω_{10}	727	$\tilde{d}_{10}$	0.20	$\tilde{d}_{10}$	0.09
ω_{11}	784	$\tilde{d}_{11}$	0.30	$\tilde{d}_{11}$	0.18
ω_{12}	833	$\tilde{d}_{12}$	0.11	$\tilde{d}_{12}$	0.03
ω_{13}	859	$\tilde{d}_{13}$	0.02	$\tilde{d}_{13}$	0.05
ω_{14}	948	$\tilde{d}_{14}$	0.06	$\tilde{d}_{14}$	0.02
ω_{15}	984	$\tilde{d}_{15}$	0.06	$\tilde{d}_{15}$	0.16
ω_{16}	1024	$\tilde{d}_{16}$	0.05	$\tilde{d}_{16}$	0.07
ω_{17}	1106	$\tilde{d}_{17}$	0.23	$\tilde{d}_{17}$	0.04
ω_{18}	1207	$\tilde{d}_{18}$	0.15	$\tilde{d}_{18}$	0.13
ω_{19}	1235	$\tilde{d}_{19}$	0.16	$\tilde{d}_{19}$	0.23
ω_{20}	1282	$\tilde{d}_{20}$	0.20	$\tilde{d}_{20}$	0.22
ω_{21}	1387	$\tilde{d}_{21}$	0.12	$\tilde{d}_{21}$	0.07
ω_{22}	1451	$\tilde{d}_{22}$	0.07	$\tilde{d}_{22}$	0.07
ω_{23}	1536	$\tilde{d}_{23}$	0.05	$\tilde{d}_{23}$	0.09
ω_{24}	1575	$\tilde{d}_{24}$	0.16	$\tilde{d}_{24}$	0.18
ω_{25}	1698	$\tilde{d}_{25}$	0.28	$\tilde{d}_{25}$	0.14
ω_{26}	1801	$\tilde{d}_{26}$	0.02	$\tilde{d}_{26}$	0.02

[a] ε_e is the electronic contribution to the energy of the i-th ES (GS energy ε_g is set to zero);

[b] spectrum origin (adiabatic transition energy) shifted to match the experimental value;

Table S2. Parameters for simulating the excited state absorption associated with the triplet $\pi\pi^*$ and $n\pi^*$ states obtained with the gradient projection method (sec. 1.3.3) using gradients of the bright excited states accessible from each state at the SS-CASPT2/SA-5-RASSCF$(12,9|2,4)$ and the ground state normal modes.

Normal mode		bright states from $^3\pi\pi^*_{\text{min}}$				bright states from $^3n\pi^*_{\text{min}}$	
			root $4^{a,d}$		root $5^{b,d}$		root $4^{c,d}$
№	ω [cm^{-1}]	$\varepsilon^e_{e/f}$ [cm^{-1}]	40415		42830	$\varepsilon^e_{e/f}$ [cm^{-1}]	40070
ω_2	160	$\tilde{d}_2$	0.42	$\tilde{d}_2$	1.47	$\tilde{d}_2$	1.66
ω_3	251	$\tilde{d}_3$	0.63	$\tilde{d}_3$	0.50	$\tilde{d}_3$	0.32
ω_4	330	$\tilde{d}_4$	0.74	$\tilde{d}_4$	0.23	$\tilde{d}_4$	0.09
ω_5	457	$\tilde{d}_5$	0.22	$\tilde{d}_5$	0.25	$\tilde{d}_5$	0.17
ω_6	467	$\tilde{d}_6$	0.35	$\tilde{d}_6$	0.20	$\tilde{d}_6$	0.02
ω_7	583	$\tilde{d}_7$	0.03	$\tilde{d}_7$	0.38	$\tilde{d}_7$	0.47
ω_8	640	$\tilde{d}_8$	0.47	$\tilde{d}_8$	0.23	$\tilde{d}_8$	0.10
ω_9	698	$\tilde{d}_9$	0.11	$\tilde{d}_9$	0.08	$\tilde{d}_9$	0.02
ω_{10}	727	$\tilde{d}_{10}$	0.17	$\tilde{d}_{10}$	0.10	$\tilde{d}_{10}$	0.09
ω_{11}	784	$\tilde{d}_{11}$	0.03	$\tilde{d}_{11}$	0.04	$\tilde{d}_{11}$	0.08
ω_{12}	833	$\tilde{d}_{12}$	0.23	$\tilde{d}_{12}$	0.04	$\tilde{d}_{12}$	0.08
ω_{13}	859	$\tilde{d}_{13}$	0.25	$\tilde{d}_{13}$	0.06	$\tilde{d}_{13}$	0.04
ω_{14}	948	$\tilde{d}_{14}$	0.10	$\tilde{d}_{14}$	0.17	$\tilde{d}_{14}$	0.18
ω_{15}	984	$\tilde{d}_{15}$	0.21	$\tilde{d}_{15}$	0.16	$\tilde{d}_{15}$	0.14
ω_{16}	1024	$\tilde{d}_{16}$	0.02	$\tilde{d}_{16}$	0.04	$\tilde{d}_{16}$	0.07
ω_{17}	1106	$\tilde{d}_{17}$	0.09	$\tilde{d}_{17}$	0.06	$\tilde{d}_{17}$	0.14
ω_{18}	1207	$\tilde{d}_{18}$	0.02	$\tilde{d}_{18}$	0.11	$\tilde{d}_{18}$	0.11
ω_{19}	1235	$\tilde{d}_{19}$	0.07	$\tilde{d}_{19}$	0.17	$\tilde{d}_{19}$	0.13
ω_{20}	1282	$\tilde{d}_{20}$	0.20	$\tilde{d}_{20}$	0.07	$\tilde{d}_{20}$	0.01
ω_{21}	1387	$\tilde{d}_{21}$	0.05	$\tilde{d}_{21}$	0.16	$\tilde{d}_{21}$	0.14
ω_{22}	1451	$\tilde{d}_{22}$	0.07	$\tilde{d}_{22}$	0.03	$\tilde{d}_{22}$	0.00
ω_{23}	1536	$\tilde{d}_{23}$	0.14	$\tilde{d}_{23}$	0.11	$\tilde{d}_{23}$	0.09
ω_{24}	1575	$\tilde{d}_{24}$	0.21	$\tilde{d}_{24}$	0.16	$\tilde{d}_{24}$	0.13
ω_{25}	1698	$\tilde{d}_{25}$	0.06	$\tilde{d}_{25}$	0.06	$\tilde{d}_{25}$	0.07
ω_{26}	1801	$\tilde{d}_{26}$	0.05	$\tilde{d}_{26}$	0.07	$\tilde{d}_{26}$	0.10

[a] TDM: 0.570 -0.143 0.364;

[b] TDM: 0.243 -0.035 0.144;

[c] TDM: 0.508 -0.150 0.324;

[d] root labeling follows the energetic order at the corresponding minimum $^3\pi\pi^*_{\text{min}}$ or $^3n\pi^*_{\text{min}}$, accounting for both the electronic contribution ϵ_f and the state-specific reorganization energy (eq. 19);

[e] $\varepsilon_{e/f}$ is the electronic contribution to the energy of the i-th ES (GS energy ε_g is set to zero);

3 Steady-State Spectroscopy

The steady-state absorption spectrum was measured at room temperature using a V-570 Jasco spectrophotometer. It was background corrected by subtracting the solvent spectrum measured at the same experimental conditions. The 4-thiouracil solution with concentration of 6 mM results in an absorbance of 2 OD at the central pump wavelength, as shown in Figure S20.

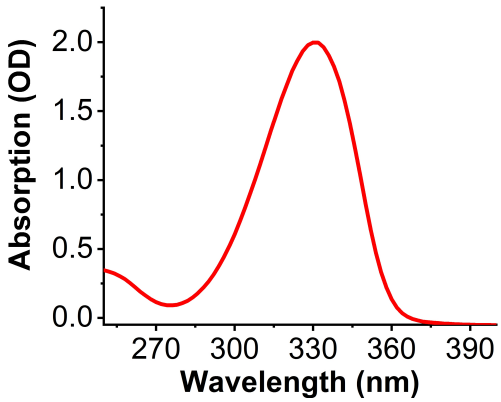

Figure S20: Linear absorption spectrum of 4-thiouracil in PBS.

4 Transient absorption spectroscopy

4.1 Transient absorption spectra

Figure S21 reports the transient spectra. A blueshift is observed for the redder wavelengths (500-700 nm), while the blue part of the spectrum (350-500 nm) is modulated by a complex oscillatory pattern (see also Figure S22).

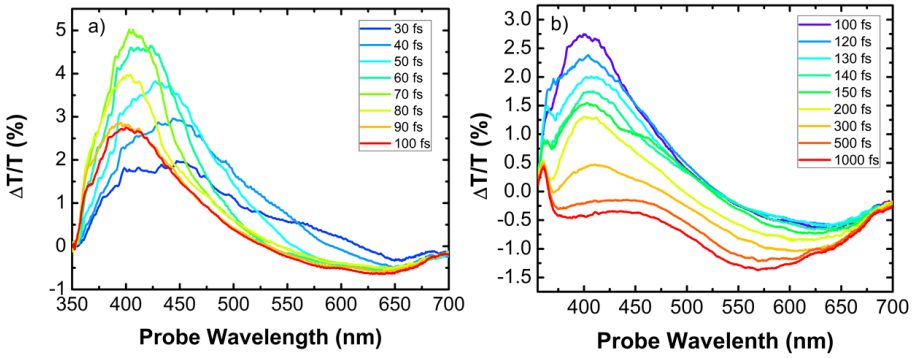

Figure S21: Transient absorption spectra in a) short and b) long timescales.

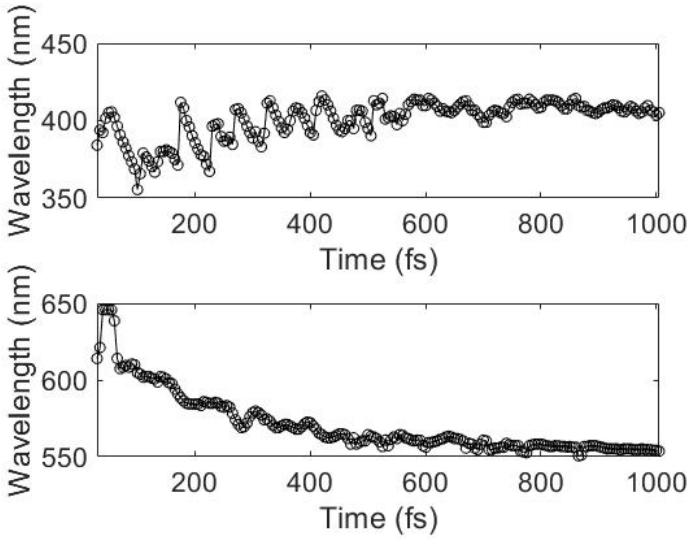

Figure S22: Temporal evolution of the wavelengths at which the maximum of the SE (upper panel) and the minimum of the PA (below) bands occur.

4.2 Global analysis

A global analysis of the data [Sto04] allows to obtain the time constants governing the dynamics over the entire dataset. A preliminary step in global analysis is to perform singular value decomposition (SVD) in order to find the number of linearly independent vectors (decay constants) significantly different from the noise. In the present work we found three dominant components and some others associated to the coherent artefact. Then a nonlinear least squares fit is performed simultaneously on these transients with exponential functions $A_i e^{-\frac{t}{\tau_i}}$. For a given time constant τ_i the decay associated spectrum (DAS) gives the wavelength dependent amplitude associated with it. The analysis takes into account also the coherent artefact, whose oscillatory time profile was modelled by a sequence of exponentials, and the dispersion due to the chirp of the probe (modelled by a third-order polynomial).

The meanings of the signs of the DAS, depending on whether they refer to positive (PA) or negative (GSB/SE) bands, are:

• Positive ΔA (PA bands): negative DAS are associated to a rise of the signal and positive DAS to a decay.

• Negative ΔA (SE bands): positive DAS related to a rise of the signal, whereas negative DAS to a decay.

4.3 Coherent oscillations

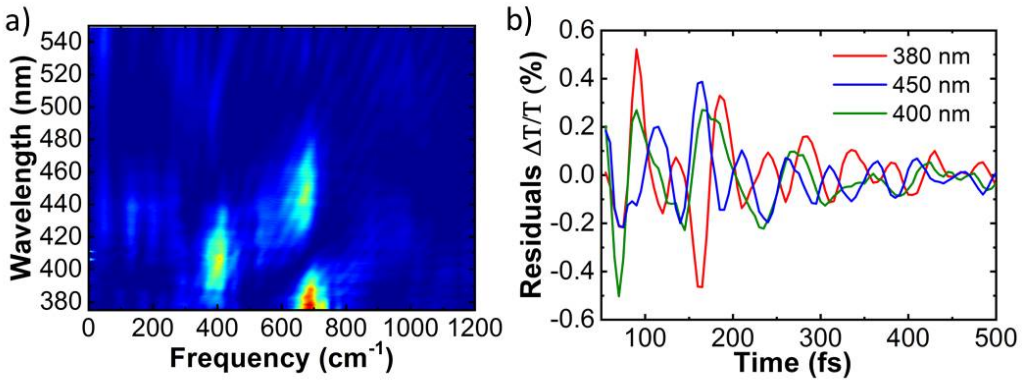

Figure S23: a) 2D Fourier transform of the residuals of the TAS measurement; b) residuals at given wavelengths.

A two-dimensional (2D) Fourier transform of the residuals of the global fit was performed to study the excited-state coherent oscillations (Figure S23a). To do so, the chirp of the probe was corrected by fitting the dispersion function and one-dimensional Fourier transform of the oscillatory components $O(\lambda_{pr}, \tau)$ was performed for each probe wavelength λ_{pr}:

$$f(\lambda_{pr}, \omega) = \int O(\lambda_{pr}, \tau) exp(-i\omega\tau) d\tau \tag{34}$$

We observe two modes at 680 and 400 cm^{-1}. At a wavelength of 400 nm (peak of the SE) the 680 cm^{-1} mode presents a minimum, whereas the 400 cm^{-1} mode is enhanced. This behaviour is associated to the wavepacket motion around the Min$\pi\pi^*$, which results on a phase flip in the oscillations (Figure S23b).

4.4 Transient absorption in the UV range

TA measurements have been performed also probing in the UV range (250-360 nm). In Figure S24 UV TA map is reported: we observe the GSB band centered at 335 nm and positive ESA signals in the deeper UV.

If we look at the dynamics in Figure (S25b), we note that GS signal shows a recovery, providing important complementary dynamical information about the population remaining in the excited states and returning to the ground state.

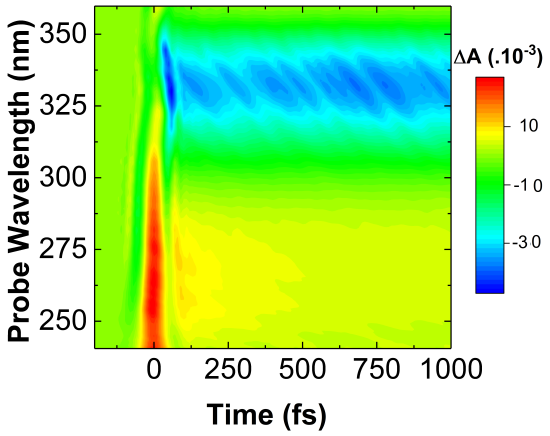

Figure S24: ΔA map of 4-thiouracil in PBS (pH 7.4) solution, probing in the UV range.

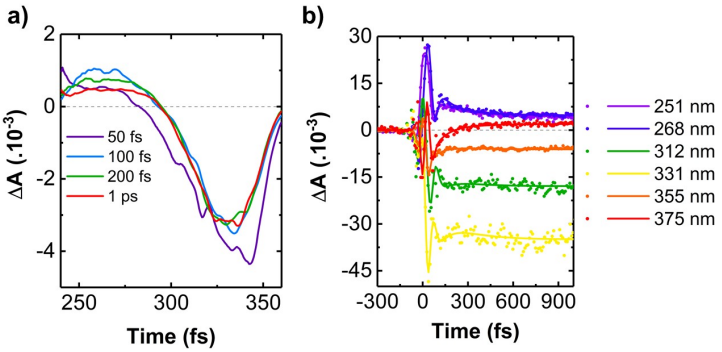

Figure S25: (a)ΔA spectra at selected pump-probe delays probing in the UV range; (b) dynamics at different probe wavelengths.

4.5 Dynamics at 600 nm for 2-thiouracil and 4-thiouracil

Figure S26 shows the transient absorption dynamics at 600 nm for the 2-thiouracil and 4-thiouracil. The traces show a decay with time constants about 406 fs and 200 fs for the triplet formation of the 2-thiouracil and 4-thiouracil, respectively.

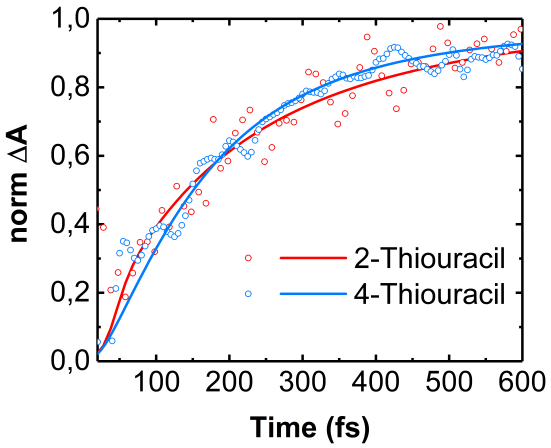

Figure S26: Dynamics at 600 nm. The red curves are for the 2-thiouracil and the blue curves are for the 4-thiouracil. The dots are the experimental data and the solid lines the exponential fits.

5 Cartesian coordinates

Min S_0

C	17.803042	18.030324	16.491376
N	18.661627	17.002731	16.231633
C	18.410827	16.057711	15.278065
C	17.318758	16.138658	14.477283
C	16.426965	17.250824	14.598700
N	16.752104	18.128950	15.609377
H	17.124179	15.377005	13.740260
S	15.077605	17.502492	13.673507
O	17.941570	18.789844	17.447464
H	19.124280	15.250151	15.226637
H	16.118840	18.911060	15.770608
H	19.485142	16.940630	16.830954

Min S_1 ($^1n\pi^*$)

C	17.784640	18.011172	16.486322
N	18.668585	17.016141	16.213425
C	18.484574	16.068783	15.209550
C	17.389047	16.182801	14.373806
C	16.504986	17.242518	14.553838
N	16.739160	18.141120	15.603012
H	17.203099	15.433819	13.619843
S	15.023214	17.471955	13.652527
O	17.896998	18.749115	17.470979
H	19.173312	15.242796	15.199138
H	16.123380	18.923950	15.791584
H	19.465438	16.972000	16.844443

Min S_2 ($^1\pi\pi$)

C	17.819666	18.024257	16.472557
N	18.684469	16.993881	16.229771
C	18.479440	15.995799	15.288763
C	17.301815	16.121072	14.466531
C	16.461367	17.212756	14.606097
N	16.770458	18.153784	15.593222
H	17.075381	15.365273	13.730795
S	15.016891	17.524932	13.696204
O	17.965927	18.780585	17.435097
H	19.175029	15.177161	15.265346
H	16.117659	18.909767	15.770729
H	19.490702	16.963273	16.855938

CI ($^1n\pi^*$ / $^1\pi\pi$)

C	17.754662	18.027106	16.484986
N	18.649314	16.947184	16.256347
C	18.523110	15.924850	15.400140
C	17.235141	16.055944	14.484947
C	16.406074	17.180292	14.608318
N	16.724656	18.133494	15.590900
H	17.031863	15.305557	13.726855
S	14.981968	17.540044	13.679208
O	17.971020	18.774311	17.455182
H	19.240262	15.109272	15.361675
H	16.041623	18.896007	15.732947
H	19.464633	16.988521	16.910987

Min $^3\pi\pi$

C	17.813563	18.038280	16.436765
N	18.683893	17.011787	16.211145
C	18.457285	15.995849	15.291382
C	17.288988	16.051565	14.528489
C	16.447394	17.146140	14.635792
N	16.807423	18.185742	15.514693
H	17.030206	15.234027	13.876175
S	15.112441	17.380037	13.558597
O	17.925660	18.786451	17.410229
H	19.112478	15.145162	15.337345
H	16.139235	18.913371	15.736423
H	19.474134	16.969911	16.850822

Min $^3n\pi$

C	17.800008	18.005642	16.453828
N	18.658631	16.964826	16.245068
C	18.420982	15.940559	15.334052
C	17.351701	16.077125	14.447552
C	16.504953	17.166243	14.552005
N	16.776238	18.127591	15.545192
H	17.183699	15.341071	13.677790
S	15.061022	17.457119	13.630422
O	17.924208	18.781810	17.403336
H	19.099186	15.105091	15.350798
H	16.095875	18.845702	15.759768
H	19.453900	16.930258	16.880131

Min S_3 ($^1\pi\pi$)

C	17.797803	17.974836	16.390006
N	18.658770	16.960925	16.203744
C	18.429770	15.954244	15.271514
C	17.292185	16.026180	14.439782
C	16.438276	17.140824	14.516521
N	16.718080	18.051483	15.527778
H	17.089701	15.229105	13.741468
S	15.000640	17.606076	13.645676
O	17.919198	18.834523	17.292868
H	19.120880	15.129815	15.280814
H	16.100805	18.850014	15.684608
H	19.471592	16.941656	16.824403

CI (S_3/S_2)

C	17.797803	17.974836	16.390006
N	18.658770	16.960925	16.203744
C	18.429770	15.954244	15.271514
C	17.292185	16.026180	14.439782
C	16.438276	17.140824	14.516521
N	16.718080	18.051483	15.527778
H	17.089701	15.229105	13.741468
S	15.000640	17.606076	13.645676
O	17.919198	18.834523	17.292868
H	19.120880	15.129815	15.280814
H	16.100805	18.850014	15.684608
H	19.471592	16.941656	16.824403

6 References

1. [Abr07] Abramavicius, D.; Valkunas, L.; Mukamel; S. Europhys. Lett. 2007, 80, 17005.
2. [Abr09] Abramavicius, D.; Palmieri, B.; Voronine, D. V.; Sanda, F.; Mukamel, S. Chem. Rev. 2009, 109, 2350-2408.
3. [But12] Butkus, V.; Valkunas, L.; Abramavicius, D. J. Chem. Phys. 2012, 137, 044513.
4. [Fer12] Ferrer, F. J. A.; Santoro, F. Phys. Chem. Chem. Phys., 2012, 14, 13549-13563.
5. [Gra07] Granucci, G.; Persico, M. J. Chem. Phys., 2007, 126, 134114.
6. [Ham11] Hamm, P.; Zanni, M. Concepts and Methods of 2d Infrared Spectroscopy; Cambridge University Press: Cambridge, U.K., 2011.
7. [Kur01] Kurtz, L.; Hofmann, A.; de Vivie-Riedle, R. J. Chem. Phys. 2001, 114, 6151-6159.
8. [Kur01b] Kurtz, L. Disseration at the LMU Müenchen, 2001.
9. [Lee16] Lee, M. K.; Huo, P.; Coker; D. F. Annu. Rev. Phys. Chem. 2016. 67:639-68.
10. [Li94] Li, B.; Johnson, A. E.; Mukamel, S.; Myers, A. B. J. Am. Chem. Soc. 1994,116, 11039-11047.
11. [Mai16] Mai, S.; Marquetand, P.; González, L. J. Phys. Chem. Lett. 2016, 7, 1978–1983.
12. [Mal86] Malmqvist, P.Å. Int. J. Quantum Chem., 1986, 30, 479-494.
13. [Mar17] Martínez-Fernández, L.; Granucci, G.; Pollum, M.; Crespo-Hernández, C. E.; Persico, M.; Corral, I. Chem. - A Eur. J. 2017, 23 (11), 2619–2627.
14. [Muk95] Mukamel, S. Principles of Nonlinear Optical Spectroscopy; Oxford University Press: New York, 1995.
15. [Muk04] Mukamel, S.; Abramavicius, D. Chem. Rev. 2004, 104, 2073-2098.
16. [Nem10] Nemeth, A.; Milota, F.; Mančal, T.; Pullerits, T.; Sperling, J.; Hauer, J.; Kauffmann, H. F.; Christensson N. J. Chem. Phys. 2010, 133, 094505.
17. [Pit09] Pittner, J.; Lischka, H,; Barbatti, M. Chem. Phys., 2009, 356, 147.
18. [Sto04] van Stokkum, I. H. M; Larsen, D. S.; van Grondelle, R. Biochim. Biophys. Acta 2004, 1657,82-104.
19. [Val16] Valkunas, L.; Abramavicius, D.; Mančal, T. Molecular Excitation Dynamics and Relaxation, Wiley-VCH Verlag GmbH & Co. KGaA, 2016.
20. [Zhu05] Zhu, C.; Jasper, A. W.; Truhlar, D. G. J. Chem. Theory Comput., 2005, 1, 527–540.